Meta-analysis

Cite
Gnaiger E (2021) Bioenergetic cluster analysis – mitochondrial respiratory control in human fibroblasts. MitoFit Preprints 2021.8. doi:10.26124/mitofit:2021-0008

Conflicts of interest
EG is founder and CEO of Oroboros Instruments, Innsbruck, Austria.

Received 2021-09-21
Accepted 2021-09-21

Online 2021-09-21
MitoFit Preprints 2021.8
doi:10.26124/mitofit:2021-0008

Data availability
Original files are available Open Access at Zenodo repository:
10.5281/zenodo.5518506

Keywords
human dermal fibroblasts, HDF
living cells, ce
cell respiration
coupling control
oxidative phosphorylation, OXPHOS
age
senescence
bioenergetic cluster analysis, BCA
meta-analysis
normalization
high-resolution respirometry, HRR
Oroboros O2k
Seahorse XF Analyzer
outlier-skewness index, *OSI*
regression analysis

Bioenergetic cluster analysis – mitochondrial respiratory control in human fibroblasts

Erich Gnaiger

Oroboros Instruments, Innsbruck, Austria

Correspondence: erich.gnaiger@oroboros.at

MitoFit Preprints 2021.8. doi:10.26124/mitofit:2021-0008

Abstract

Cell respiration reflects mitochondrial fitness and plays a pivotal role in health and disease. Despite the rapidly increasing number of applications of cell respirometry to address current challenges in biomedical research, cross-references are rare between respirometric projects and platforms. Evaluation of accuracy and reproducibility between laboratories requires presentation of results in a common format independent of the applied method. When cell respiration is expressed as oxygen consumption rate in an experimental chamber, normalization is mandatory for comparability of results. Concept-driven normalization and regression analysis are key towards bioenergetic cluster analysis presented as a graphical tool to identify discrete data populations.

In a meta-analysis of human skin fibroblasts, high-resolution respirometry and polarography covering cell senescence and the human age range are compared with multiwell respirometry. The common coupling control protocol measures ROUTINE respiration of living cells followed by sequential titrations of oligomycin, uncoupler, and inhibitors of electron transfer.

ROUTINE respiration, *R*
LEAK respiration, *L*
electron transfer capacity, *E*
residual oxygen consumption, *Rox*
L/*E* flux control ratio
net *E*, *netE* = *E*-*L*
E-*L* coupling efficiency, $j_{E\text{-}L}$ = (*E*-*L*)/*E* = 1-*L*/*E*
R/*E* flux control ratio
reserve *E*, *resE* = *E*-*R*
E-*R* reserve efficiency, $j_{E\text{-}R}$ = (*E*-*R*)/*E* = 1-*R*/*E*
net *R*, *R*-*L*
net *R*-*L* control ratio, (*R*-*L*)/*E*

Bioenergetic cluster analysis increases the resolution of outliers within and differences between groups. An outlier-skewness index is introduced as a guide towards logarithmic transformation for statistical analysis. *Isolinear* clusters are separated by variations in the extent of a quantity that correlates with the rate, whereas *heterolinear* clusters fall on different regression lines. *Dispersed* clusters are clouds of data separated by a critical threshold value. Bioenergetic cluster analysis provides new insights into mitochondrial respiratory control and a guideline for establishing a quality control paradigm for bioenergetics and databases in mitochondrial physiology.

Graphical abstract – Bioenergetic cluster analysis BCA. Normalization of respiration (O_2 flux) is graphically represented in *Y*/*X* plots and evaluated by regression analysis, considering variances of the reference variable and O_2 flux. Selection of a reference O_2 flux as the reference in a particular respiratory state yields normalization independent of measurements of cell volume, protein mass, or mitochondrial markers. Regression analysis is applied for distinguishing isolinear, heterolinear and dispersed clusters in BCA for outlier characterization and corresponding evaluation of mitochondrial respiratory control in diagnostic groups.

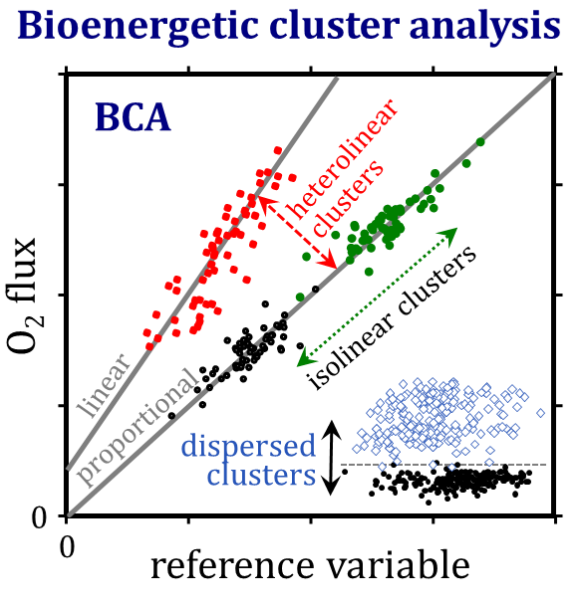

1. Introduction

Upon compromise of mitochondrial functional fitness, cell respiration and energy metabolism are impaired with a negative impact on quality of life, healthy aging, and resistance to degenerative diseases and immunological disorders (Wallace et al 2010; Nunnari, Suomalainen 2012; Herst et al 2017; Annesley, Fisher 2019). Physical exercise and a caloric balanced lifestyle stimulate mitochondrial biogenesis and quality control in muscle tissue and provide a systemic nonpharmacological intervention to prevent mitochondrial dysfunction that is prevalent in many conditions such as obesity (de Mello et al 2018; Han et al 2019; Hood et al 2019; Memme et al 2021). Complementary to research on isolated mitochondria and permeabilized cells or tissues, experiments with living cells play a key role in biomedical research and diagnostic studies of

mitochondrial diseases. Therefore, cultured human cell lines provide an alternative to invasive biopsies and animal testing, which needs critical evaluation (Schöpf et al 2020).

Respiratory control in living cells is studied by sequential measurement of ROUTINE respiration *R*, oligomycin-inhibited LEAK respiration *L* (this step may be omitted as a control), uncoupler-stimulated electron transfer (ET) capacity *E*, and residual oxygen consumption *Rox* after inhibition of ET by rotenone and antimycin A (Steinlechner-Maran et al 1996; Villani, Attardi 1997; Renner et al 2003; Hütter et al 2004; Wu et al 2007; Gnaiger 2020). Respirometric coupling control protocols in living cells are carried out in cell culture media or mitochondrial respiration media which may be supplemented by respiratory fuel substrates (Karabatsiakis et al 2014; Doerrier et al 2018). The term 'mitochondrial stress test' (Jaber et al 2020) is used synonymously for the original coupling control or phosphorylation control protocol (Gnaiger 2008). Despite of considerable standardization of these substrate-uncoupler-inhibitor titration (SUIT) protocols, surprisingly few compilations and comparisons are available of quantitative respirometric results on living cells studied in different projects and laboratories, and by application of different instrumental platforms (Wagner et al 2011; Mahapatra et al 2018; Gnaiger 2020; Zdrazilova et al 2021). Respiratory rates normalized for sample-specific attributes are open for meta-analyses to address research topics beyond the restraints of a particular experiment (Gnaiger et al 2020).

This meta-analysis focuses on respiration of human dermal fibroblasts. The effect of donor age on mitochondrial respiratory control (Greco et al 2003) is contrasted with the specific pathophysiology of cell senescence (Hütter et al 2004) by distinguishing the repercussions of ET capacity versus coupling in oxidative phosphorylation (OXPHOS) on the efficiency of mitochondrial energy transformation. A large data set on neonatal normal human dermal fibroblasts (Yépez et al 2018) is compared with neonatal healthy control cells (Zdrazilova et al 2021). Bioenergetic cluster analysis (BCA) is introduced as a general framework for characterization of mitochondrial respiratory control in living cells. BCA can be extended to the analysis of all cell types and OXPHOS studied with a variety of SUIT protocols in isolated mitochondria, permeabilized cells and tissues, and tissue homogenates (Gnaiger 2020). Transparent and traceable evaluation of outliers is key in addressing the reproducibility crisis. Beyond mere statistical outlier detection, BCA identifies bioenergetic features of outliers as a diagnostic step towards solving underlying limitations causing the generation of outliers.

2. Conceptual background

2.1. Concept-driven normalization

> '*The challenges of measuring mitochondrial respiratory rate are matched by those of normalization*' (Gnaiger et al 2020).

The oxygen consumption rate OCR is frequently reported as O_2 consumption in the experimental system (chamber or well) per unit of time, I_{O2} [mol·s^{-1}]. For quantitative comparison, respirometric data must be (*1*) represented as normalized quantities, (*2*) referred to defined respiratory states, and (*3*) expressed in identical units.

Normalization of cell respiration by cell count integrates — thus does not distinguish between — the effects of (*1*) cell size, (*2*) mitochondrial (mt) density, and (*3*) mt-quality on respiratory capacity (Renner et al 2003; Hütter et al 2004). Mitochondrial markers are used for normalization of respiration to obtain quantities that are independent of cell size and mt-density (Table 1).

A normalization can be represented as a Y/X plot. The reference is plotted on the *x*-axis or abscissa as the independent variable X. The rate is plotted on the *y*-axis or ordinate as the dependent variable Y (Figure 1a). Frequently, neither reference nor rate are independent. A flux control ratio is obtained when the reference is a rate in a different state, independent of cell count, cell size and mitochondrial density. Flux control ratios and flux control efficiencies are normalizations calculated from rates measured in a sequence of respiratory states in a SUIT protocol (Gnaiger 2020). For example, a plot of ROUTINE respiration as a function of ET capacity represents the dimensionless R/E flux control ratio FCR. The reference rate (E) in a FCR is considered as an internal functional mt-marker mtE for the rate in any respiratory state i (Table 1),

$$FCR = J_{O_2/mtE} = \frac{I_{O_2}(\text{state } i)}{I_{O_2}(\text{reference state})} \quad \text{Eq. 1}$$

The choice of an appropriate reference state is neither absolute nor entirely arbitrary and may be dictated by the research question. A numerically driven definition of the reference state as the maximum rate yields normalized flux control ratios in the range of 0 to 1. Conceptually, it is decisive to consider the intercept when the reference variable is extrapolated to zero (Figure 1). R and L depend on the ET capacity. At ET capacity E = 0, therefore, both R and L are zero by definition, in agreement with experimental evidence (see Results, Figures 7*R* and 8). LEAK respiration may theoretically decline to zero at positive E and R, which is observed empirically (see Results, Figures 7*L* and 11a). In a linear but not proportional function,

$$R = b \cdot L + a \quad \text{Eq. 2}$$

the intercept a is equal to ROUTINE respiration when L is extrapolated to zero. Consequently, the slope b is the constant ratio,

$$b = \frac{R-a}{L} \quad \text{Eq. 3}$$

In contrast, R/L is neither a constant at variable R (Eq. 2) nor a concept-driven ratio, even if frequently applied — compare the classical respiratory adenylate control ratio RCR ~ P/L. OXPHOS capacity P is determined at kinetically saturating concentrations of ADP and inorganic phosphate which cannot be obtained in living cells but requires mt-preparations (for definitions, see Gnaiger et al 2020).

The ratio of ROUTINE respiration and ET capacity is the R/E flux control ratio (Eq. 1), simply related to the *E*-*R* reserve efficiency $j_{E\text{-}R}$, as is the L/E flux control ratio related to the *E*-*L* coupling efficiency $j_{E\text{-}L}$ (Gnaiger 2020),

E-*R* reserve efficiency $$j_{E-R} = \frac{E-R}{E} = 1 - \frac{R}{E} \quad \text{Eq. 4a}$$

E-*L* coupling efficiency $$j_{E-L} = \frac{E-L}{E} = 1 - \frac{L}{E} \quad \text{Eq. 4b}$$

The *E-R* reserve efficiency is under physiological control by intermediary metabolism and cellular aerobic energy demand and is regulated by the *E-L* coupling efficiency.

The slope between O_2 flow I_{O2} and the cell count (number of cells N_{ce} [x]) in the chamber yields O_2 flow per cell $I_{O2/ce}$ (Gnaiger et al 2020),

$$I_{O_2/ce} = \frac{I_{O_2}}{N_{ce}} \quad [amol \cdot s^{-1} \cdot x^{-1}] \quad \text{Eq. 5}$$

On the other hand, the slope between I_{O2} and total cell size — e.g. expressed as cell volume V_{ce} [pL] in the chamber — yields cell-volume specific O_2 flux $J_{O2/Vce}$,

$$J_{O_2/V_{ce}} = \frac{I_{O_2}}{V_{ce}} \quad [amol \cdot s^{-1} \cdot pL^{-1}] \quad \text{Eq. 6}$$

If V_{ce} is varied by changing the number of identical cells in the chamber, the relation between I_{O2} and V_{ce} is linear and proportional (zero intercept) in the absence of a crowding effect and within limits of linearity of the respirometric instrument. The cell volume V_{ce} in the chamber is distinguished from the volume per cell $V_{U_{ce}}$ (volume per elementary unit U_{ce} [x]; x is the unit of count) (Gnaiger 2020; 2021),

$$V_{U_{ce}} = \frac{V_{ce}}{N_{ce}} \quad [pL \cdot x^{-1}] \quad \text{Eq. 7}$$

O_2 flow $I_{O2/ce}$ (per cell) scales with $V_{U_{ce}}$ and total body mass according to allometric relations (Miettinen, Björklund 2017; Savage et al 2007). Different research questions are addressed by specific concept-driven normalizations, which are distinguished as extensive, specific, and kinetic or intensive (Table 1).

Table 1. Concepts of normalization of O_2 consumption. Relations of O_2 consumption to reference attributes are categorized in the footnotes.

Extensive[a] $I_{O2} \rightarrow I_{O2/ce}$	**Size-specific**[b] $I_{O2/ce} \rightarrow J_{O2/Quce}$	**mt-specific**[a] $I_{O2/ce} \rightarrow J_{O2/mtE}$	**Kinetic or intensive**[c]
cell count N_{ce}	volume per cell $V_{U_{ce}}$	mt-volume $V_{U_{mt}}$	substrate concentration c_X
	mass per cell $M_{U_{ce}}$	mt-membrane area	mt-membrane potential $\Delta\Psi_p^+$
	cell-marker enzyme	mt-marker enzyme	protonmotive force *pmF*
	cell protein	reference rate	protonmotive pressure $\Delta_m\Pi_p^+$

[a]linear; [b]linear or logarithmic; [c]hyperbolic (c_X), non-linear ($\Delta\Psi_p^+$ and *pmF*), linear ($\Delta_m\Pi_p^+$; Gnaiger 2020)

Even if information is available on cell volume and cell protein as markers of cell size, and citrate synthase CS activity is measured as a mt-marker (Renner et al 2003; Greco et al 2003; Hütter et al 2004), comparison with other studies (Yépez et al 2018) is restricted to normalization of respiration by cell count and marker-independent flux ratios and flux control efficiencies. Variability of results on attributes used for external normalization may override variability of measurements of respiratory rates. BCA and regression analysis of flux ratios avoid the consequence of discrepancies at more than one order of magnitude in interlaboratory tests on activities of respiratory Complexes, CS, and total protein mass (Gellerich et al 2004).

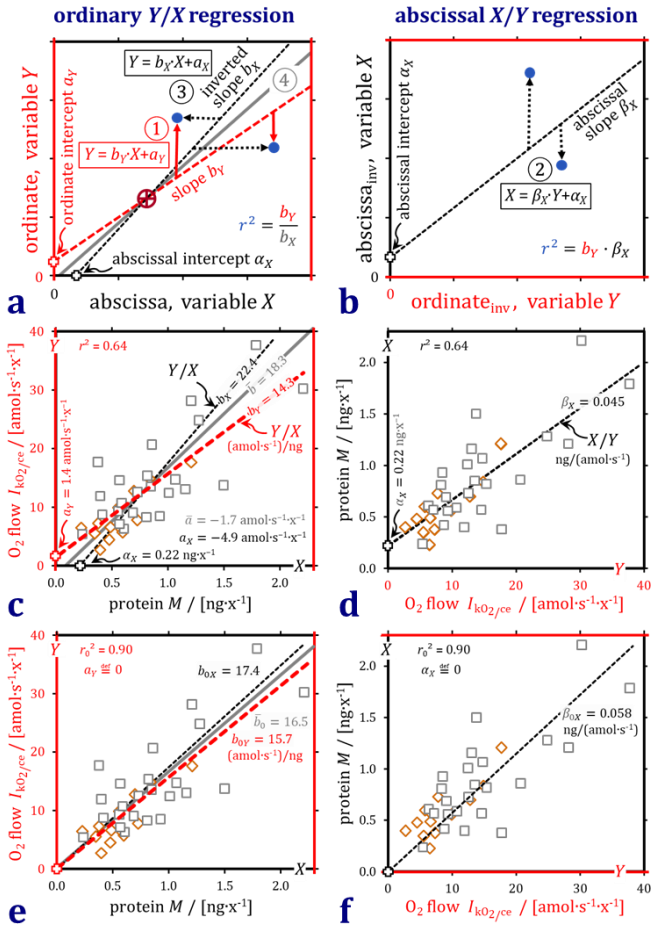

Figure 1. Inversion of axes in regression analysis. (a) and **(b)** Scheme of inverted regression analysis. ① Ordinary Y/X least-squares regression; minimized residuals on Y (vertical full arrows; b_Y and a_Y). ② Abscissal regression with inverted axes; minimized residuals on X (vertical dotted arrows; β_X and α_X). ③ Ordinate projection of abscissal regression with inverted parameters, $b_X = 1/\beta_X$ and $a_X = -\alpha_X/\beta_X$. ④ Mean regression line with parameters $\bar{b}$ and $\bar{a}$. Crossover point ⊕ between Y/X and X/Y regression lines (Table 2). **(c)** LEAK respiration $I_{O2/ce}$ of human skin fibroblasts HSF as a function of protein mass per cell M. Donor age 1-42 y (diamonds), 59-103 y (squares). Thick dashed line: slope b_Y and intercept a_Y calculated from Y/X regression. Thin dashed line: slope b_X and intercept a_X calculated from abscissal X/Y regression in panel **d**. **(d)** Data from panel **c** with inverted axes, since respiration and protein mass are measurements with experimental error. **(e)** and **(f)** Proportional regressions (through the origin) consistent with the slopes in panel **c** bracketing the zero intercept, and with theoretical extrapolations to zero protein resulting in zero respiration. Proportional regression results in a higher value of r_0^2 and a correspondingly smaller effect of axes inversion on the proportional slopes b_{0Y} and b_{0X}. Raw data: Greco et al (2003).

2.2. Inverted regression analysis

> '*.. a visual inspection of a graphic showing the interaction between two variables is often a quicker and more reliable way to detect outliers in your data than a statistical test*' (Silver 2012).

In ordinary Y/X regression, the uncertainty (error) of the values of X is assumed to be negligible. In Eq. 5, for example, X can be varied accurately in a series of dilutions at non-random intervals, whereas Y is measured as O_2 flow with experimental error. Then the ordinate intercept a_Y and slope b_Y are calculated to minimize the deviations or residuals of Y from the regression line, considering exclusively ordinate (vertical) deviations in Y in the Y/X plot. In many regression analyses — such as Eq. 2 —, however, both variables in X and Y are measurements with inherent errors. In this case it is

necessary to minimize residuals for both Y and X. To do so, the ordinate intercept a_Y and slope b_Y are calculated for the Y/X regression using ordinary least squares (Figure 1a), whereas the abscissal intercept α_X and slope β_X are obtained for the inverted X/Y regression using abscissal least squares (Figure 1b). To transpose the X/Y plot (Figure 1b) to the Y/X plot, the inverted parameters a_X and b_X are calculated from α_X and β_X (Figure 1a),

inverted intercept: $$a_X = \frac{-\alpha_X}{\beta_X}$$ Eq. 8a

inverted slope: $$b_X = \frac{1}{\beta_X}$$ Eq. 8b

Table 2. Quantities and symbols in inverted regression analysis.

Quantity	Symbol	Definition	Minimized residuals
ordinate Y/X intercept on Y	a_Y	ordinary regression	Y variable
ordinate Y/X slope	b_Y	ordinary regression	Y variable
abscissal X/Y intercept on X	α_X	abscissal regression	X variable
abscissal X/Y slope	β_X	abscissal regression	X variable
inverted Y/X intercept on Y	a_X	$a_X = -\alpha_X/\beta_X$	X variable
inverted Y/X slope	b_X	$b_X = 1/\beta_X$	X variable
mean Y/X intercept on Y	$\bar{a}$	$\bar{a} = (a_Y+a_X)/2$	Y and X variables
mean Y/X slope	$\bar{b}$	$\bar{b} = (b_Y+b_X)/2$	Y and X variables
cross-over point on X	X^*	$X^* = \frac{a_Y - a_X}{b_X - b_Y}$	
cross-over point on Y	Y^*	$Y^* = \frac{a_Y \cdot b_X - a_X \cdot b_Y}{b_X - b_Y}$	
coefficient of determination	r^2	$r^2 = b_Y/b_X = b_Y \cdot \beta_X$	Y and X variables

In Y/X regression with errors in Y and X, intercept $\bar{a}$ and slope $\bar{b}$ are the means of the Y/X and X/Y regression parameters (Table 2). The ordinate intercept a_Y yields an overestimate and the slope b_Y an underestimate (Figure 1c and d). The mean intercept $\bar{a}$ and mean slope $\bar{b}$ minimize the residuals not only in the dependent variable Y but also in the independent variable X. This is in line with the concept of the coefficient of determination r^2, which is independent of axis inversion.

Like r^2, the inverted slope ratio b_Y/b_X is always positive in the range of 0 to 1. In fact, these parameters are equal (Figure 2),

$$\frac{b_Y}{b_X} = b_Y \cdot \beta_X = r^2$$ Eq. 9

Proportional regression — known as regression through the origin — is controversial (Eisenhauer 2003) and depends on (*1*) how close the data are distributed towards the zero intercept, (*2*) testing for $a_Y>0$ and $\alpha_X>0$ (or $a_X<0$), and (*3*) a theoretical prediction that Y must be zero when $X=0$. These criteria are fulfilled, for example, in the

plot of LEAK respiration per cell as a function of protein mass per cell (Figure 1c to f). Proportional regression increases the value of r^2 to r_0^2 (using Excel), and thus diminishes the bias of the ordinate slope b_{0Y} compared to the mean slope $\bar{b}_0$ (Figure 1e). The mean proportional slope $\bar{b}_0$ can be compared with the median of the individually normalized quantities. $\bar{b}_0$ = 16.5 amol·s^{-1}·ng^{-1} (Figure 1e) is like the median protein-specific O_2 flux $J_{O2/M}$ = 16.9 amol·s^{-1}·ng^{-1}.

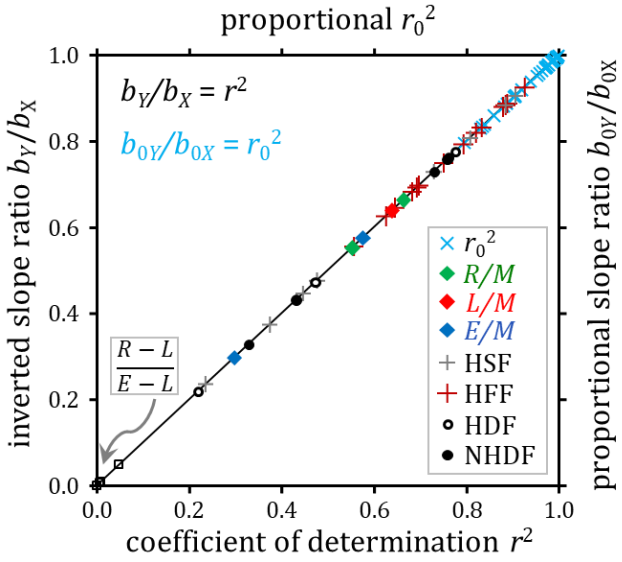

Figure 2. Equality of the inverted slope ratio b_Y/b_X and coefficient of determination r^2. Empirical values from Figures 7, 8 and 11, where b_Y and b_X are plotted as regression lines for visualization of the magnitude of r^2. Diamonds are from O_2 flow as a function of HSF cell mass (Figure 1 and 6). Corresponding proportional r_0^2 calculated by Excel and b_{0Y}/b_{0X} are higher than r^2. *R-L* is constant and independent of variations in *E-L* with near-zero r^2 (Figure 11c).

Plots of b_Y and b_X provide a direct graphical representation of the magnitude of r^2 or r_0^2 (Figure 1c and e). More advanced statistical methods are required for estimation of probabilities when considering data distribution with heteroscedasticity (Wilcox 2015). Without complete knowledge of the history of statistics it is impossible to say whether finding the equality of r^2 and the inverted slope ratio (Figure 2) is an original discovery or a re-discovery of a neglected fundamental relationship.

2.3. Outlier-skewness index

An outlier-skewness index *OSI* is defined for evaluation of the distribution of data sets with outliers including separate clusters or skewness in relation to a normal distribution with equivalence of the average and median. The *OSI* is derived from the Pearson 2 index of skewness *PSI* (Doane, Seward 2011) which relates the difference between average $\bar{x}$ and median $\tilde{x}$ to the standard deviation SD,

$$PSI = \frac{\bar{x}-\tilde{x}}{\mathrm{SD}} \cdot 3 \qquad \text{Eq. 10}$$

The outlier-skewness index *OSI* extends the *PSI* by introducing the absolute value of the arithmetic mean $\bar{m}$,

$$\bar{m} = \frac{|\bar{x}+\tilde{x}|}{2} \qquad \text{Eq. 11}$$

for normalization,

$$OSI = \frac{\bar{x}-\tilde{x}}{\bar{m} + \mathrm{SD}} = \frac{\bar{x}-\tilde{x}}{|\bar{x}+\tilde{x}|/2 + \mathrm{SD}} \qquad \text{Eq. 12}$$

At the limit of a zero value of $\bar{m}$, the O*SI* equals the *PSI* (without the multiplication factor of 3). At high $\bar{m}$ and small SD, the O*SI* approximates the difference between the average and the median normalized for $\bar{m}$, $(\bar{x} - \tilde{x})/\bar{m}$. At positive *OSI* when $\bar{x} > \tilde{x}$, skewed distribution may be shifted to a normal distribution by log-transformation (Table 3). μ and σ are the average (or median) and standard deviation of the log-transformed data. The upper and lower $\pm\sigma$ boundaries are,

$$up = \exp(\mu + \sigma) \quad \text{Eq. 13a}$$

$$low = \exp(\mu - \sigma) \quad \text{Eq. 13b}$$

Then σ is expressed on the natural scale as SD_{ln}, which yields comparability with SD of data sets analyzed without log-transformation,

$$SD_{ln} = \frac{up - low}{2} \quad \text{Eq. 14}$$

Medians are invariant in the natural and logarithmic scale after log-natural re-transformation.

3. Results

3.1. ROUTINE respiration and coupling control in living cells

Respiratory control in human fibroblasts is represented by four studies with different instrumental configurations (Tables 3 and 4). The ROUTINE state is defined as the near-physiological state of respiration *R* in living cells, without interference by externally applied inhibitors and uncouplers. *R*, *L* and *E* are O_2 fluxes linked to the mitochondrial electron transfer system ETS and thus are corrected for *Rox* determined after inhibition of the ETS (Gnaiger 2020).

The effect of cell size on cell respiration is apparent when contrasting respiration normalized for cell count in young proliferating human foreskin fibroblasts YP-HFF and senescent human foreskin fibroblasts S-HFF with volumes per cell of 2.6 and 9.9 $pL \cdot x^{-1}$, respectively (Figure 3a and b). The *R*-*L* net ROUTINE capacity and $(R\text{-}L)/E$ control ratio consider LEAK respiration *L* as a bioenergetic baseline (Figure 3), above which electron transfer to O_2 is available for oxidative phosphorylation of ADP to ATP, whereas *L* is related to the O_2 requirement for maintaining the protonmotive force by compensation of proton leak and slip and cation cycling.

Respiration is compared in YP-HFF and normal human dermal fibroblasts NHDF (Figure 3a and c). The Seahorse XF Analyzer displays O_2 consumption rates during consecutive time periods of 4-5 min as a data point separated by 2 to 4 min for reoxygenation (Wu et al 1997). Evaluation of the time periods differs according to respiratory state (Yépez et al 2018). After exclusion of outliers by bioenergetic cluster analysis (Section 3.3), ROUTINE respiration in R1 and R2 is 11 % and 3 % higher than in R3 (Figure 3c). LEAK respiration in L1, L2 and L3 is 23 %, 13 % and 6 % higher, respectively, than flow taken as the minimum in either L1, L2 or L3. ET capacity declines from E1 to E3 by 15 %. This illustrates the importance of clarification and standardization of data analysis of time intervals. Measurement of respiratory capacities

requires evaluation of steady states (Gnaiger 2001; Gnaiger et al 2020), achieved in the O2k by continuous monitoring of rate over time at 2-s data recording intervals, and steady-state sections are selected for calculation of numerical results (Figure 3d).

Table 3. Respiration *R*, *L* and *E* corrected for baseline *Rox*, and *Rox* in fibroblast cell cultures used as controls. O_2 flow normalized for cell count, 37 °C.

Cell line Instrument		ROUTINE *R* [amol·s^{-1}·x^{-1}]	LEAK *L* [amol·s^{-1}·x^{-1}]	ET capacity *E* [amol·s^{-1}·x^{-1}]	baseline *Rox* [amol·s^{-1}·x^{-1}]
YP-HFF[1]	median $\tilde{x}$	39	15	109	8
O2k 2 mL	$\bar{x}$ ± SD	38 ± 8	15 ± 4 *a*	112 ± 24	8 ± 3
	$\tilde{x}$±SD range	31 to 47	11 to 19 *a*	85 to 133	5 to 12
n=12	*OSI*	-0.02	0.04*b*	0.02	0.01
HDF[2]	median $\tilde{x}$	37	6	77	2
O2k 0.5 mL	$\bar{x}$ ± SD	37 ± 7	6 ± 3	79 ± 14	2 ± 1
	$\tilde{x}$±SD range	30 to 44	4 to 9	63 to 91	0 to 3
N=3 × *n*=4	*OSI*	0.00	-0.06	0.02	-0.01
NHDF[3]	median $\tilde{x}$	37	6	78	11
XF96	$\bar{x}$ ± SD	37 ± 12 *a*	6 ± 3 *a*	78 ± 26 *a*	10 ± 5
multiwell	$\tilde{x}$±SD range	27 to 51 *a*	3 to 9 *a*	56 to 107 *a*	6 to 17
n=2630	*OSI*	0.04*c*	0.05*c*	0.04*c*	0.02
Y-HSF[4]	median $\tilde{x}$	46	7	69	
1 to 42 years	$\bar{x}$ ± SD	49 ± 24 *a*	7 ± 4 *a*	71 ± 46 *a*	
Gilson 1.5 mL	$\tilde{x}$±SD range	28 to 75 *a*	4 to 11 *a*	37 to 130 *a*	
N=13	*OSI*	0.11*d*	0.13*d*	0.12*d*	
A-HSF[4,5]	median $\tilde{x}$	55	13	72	
59 to 103 years	$\bar{x}$ ± SD	60 ± 22 *a*	13 ± 7 *a*	77 ± 30 *a*	
Gilson 1.5 mL	$\tilde{x}$±SD range	37 to 80 *a*	8 to 21 *a*	48 to 109 *a*	
N=24	*OSI*	0.12*e*	0.09*e*	0.10*e*	

1: Young proliferating human foreskin fibroblasts (Hütter et al 2004); no outliers.
2: Neonatal and healthy patient-derived human skin fibroblasts (Zdrazilova et al 2021); *N* cell lines with *n* repeats per cell line, the cell lines were pooled; no outliers.
3: Normal human dermal fibroblasts (Yépez et al 2018); 6.8 % outliers removed.
4: Human skin-derived fibroblasts from young (Y-HSF) or aged donors (A-HSF) (Greco et al 2003). The term 'antimycin-sensitive' respiration suggests that rates were baseline corrected for *Rox*. Results on *Rox* are not available; no outliers.
5: 20.0 % outliers removed with $E \geqq R$.
a: At outlier-skewness index *OSI*>0.03 (Eq. 12), data were log-transformed; average $\bar{x}$ and SD re-transformed to the linear scale (Eq. 14).
b: log-transformation lowered the *OSI* to 0.02.
c: log-transformation lowered the *OSI* to 0.00, -0.02 and 0.00, respectively.
d: log-transformation lowered the *OSI* to 0.04, 0.06 and 0.02, respectively.
e: log-transformation lowered the *OSI* to 0.07, 0.01 and 0.04, respectively.

Table 4. Flux control ratios and flux control efficiencies normalized for ET capacity. E'_{tot} is the apparent ET capacity not corrected for *Rox*. For details see Table 3.

Cell line Instrument		ROUTINE *R/E*	net ROUTINE *(R-L) /E*	coupling efficiency *(E-L)/E*	baseline Rox/E'_{tot}
YP-HFF	median $\tilde{x}$	0.34	0.20	0.86	0.09
O2k 2 mL	$\bar{x}$ ± SD	0.34 ± 0.02	0.20 ± 0.02	0.86 ± 0.02	0.07 ± 0.03
	$\tilde{x}$±SD range	0.32 to 0.37	0.19 to 0.22	0.84 to 0.88	0.06 to 0.12
n=12	*OSI*	0.01	0.01	-0.00	-0.19
HDF	median $\tilde{x}$	0.46	0.40	0.92	0.02
O2k 0.5 mL	$\bar{x}$ ± SD	0.47 ± 0.04	0.40 ± 0.03	0.93 ± 0.03	0.02 ± 0.02
	$\tilde{x}$±SD range	0.42 to 0.50	0.36 to 0.43	0.89 to 0.96	0.00 to 0.04
N=3 × *n*=4 [a]	*OSI*	0.02	0.00	0.00	-0.04
NHDF	median $\tilde{x}$	0.47	0.40	0.93	0.12
XF96	$\bar{x}$ ± SD	0.48 ± 0.08	0.40 ± 0.07	0.92 ± 0.03	0.12 ± 0.04
	$\tilde{x}$±SD range	0.40 to 0.55	0.33 to 0.47	0.90 to 0.95	0.08 to 0.16
n=2630	*OSI*	0.01	0.01	-0.00	0.00
Y-HSF	median $\tilde{x}$	0.71	0.58	0.90	
1 to 42 y	$\bar{x}$ ± SD	0.70 ± 0.12	0.58 ± 0.07	0.88 ± 0.08	
Gilson	$\tilde{x}$±SD range	0.59 to 0.82	0.51 to 0.66	0.83 to 0.98	
N=14 [b]	*OSI*	-0.01	-0.01	-0.02	
A-HSF	median $\tilde{x}$	0.82	0.61	0.83	
59 to 103 y	$\bar{x}$ ± SD	0.78 ± 0.12	0.59 ± 0.08	0.81 ± 0.08	
Gilson	$\tilde{x}$±SD range	0.69 to 0.94	0.53 to 0.70	0.75 to 0.91	
N=26 [b]	*OSI*	-0.04	-0.03	-0.02	

a: *N* cell lines with *n* repeats per cell line, the cell lines were pooled.
b: *N* is higher than in Table 3 since flux control ratios and control efficiencies do not depend on reported protein mass.

For further comparison, ROUTINE respiration measured with the O2k in human fetal lung fibroblasts is 32±9 amol·s^{-1}·x^{-1} (Djemek et al 2018), which corresponds to results for young proliferating HFF, HDF and NHDF cells (Table 3). In contrast, Kuffner et al (2020) report 18±1 and 37±2 "pmol/min/1000 cells" for ROUTINE respiration and ET capacity, respectively, in skin fibroblasts derived from young healthy controls and measured with the XFp Flux Analyzer (possibly not background-corrected for *Rox*). This converts to 309 and 617 amol·s^{-1}·x^{-1} or eight times higher than in NHDF (Table 3). For conversion of units, see Tables 6 and 7 in Gnaiger et al (2020).

The outlier-skewness index *OSI* was >0.03 for *R*, *L*, and *E* in the large data set of NHDF, consistent with a log-transformation to obtain symmetric distribution for statistical analysis (Yépez et al 2018). In contrast, *OSI*<0.03 applied to respiration of HDF and most data on HFF, which were thus symmetrically distributed, as were the flux control ratios and flux control efficiencies of NHDF and HFF (Figure 4). Taken together, these results suggest that |*OSI*|>0.03 is the critical value indicative of unsymmetrically distributed data due to outliers, outlier clusters, or skewed distribution.

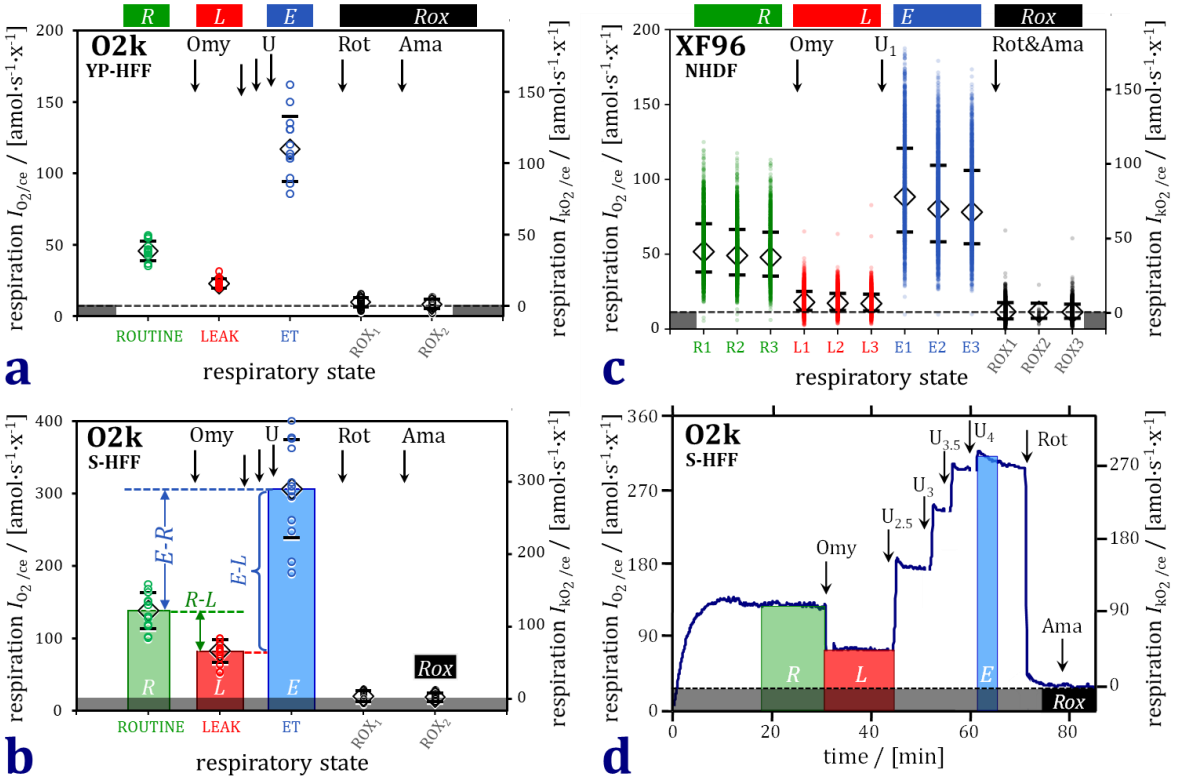

Figure 3. Respiration of fibroblasts with the coupling control protocol for living cells. ROUTINE respiration *R*, LEAK respiration *L* after inhibition of ATP synthase by oligomycin Omy, ET capacity *E* after uncoupling (U), and residual oxygen consumption *Rox* after inhibition of Complexes I and III by rotenone (Rot) and antimycin A (Ama). I_{kO2} is the *Rox*-corrected catabolic O_2 flow normalized for the cell count. **(a)** and **(b)** Scatter plots for young proliferating human foreskin fibroblasts YP-HFF and senescent human foreskin fibroblasts S-HFF measured in the O2k (calculated from raw data in Hütter et al 2004). O_2 flow normalized for cell count concentration in the stock suspension (1.0 ± 0.2 Mx·mL^{-1} and 0.20 ± 0.02 Mx·mL^{-1} in YP-HFF and S-HFF, respectively) with complete volume replacement. Results of 12 individual chambers (open circles), medians (open diamonds) ±SD (bars). Omy at 1 µg/mL (1.25 µM). *E* is the maximum respiration obtained after multiple uncoupler titrations. Median *R*, *L* and *E* are highlighted by columns in panel b. **(c)** Scatter plot for normal human dermal fibroblasts NHDF measured in the XF96 (calculated from raw data in Yépez et al 2018). Three time intervals of respiration per respiratory state (R1, R2, R3; L1, L2, L3; etc.). Omy at 1 µM. Single uncoupler titration of 1 µM FCCP. *Rox* measured in the presence of Rot&Ama. O_2 flow normalized for the seed cell count (0.02 Mx per well). 2630 data points (dots) after elimination of outliers; medians (open diamonds) ± SD_{ln} of log-transformed data converted to the natural scale resulting in non-symmetrical boundaries (bars). **(d)** Continuous trace of respiration of S-HFF measured in the O2k. Stepwise uncoupler titration from 2.5 to 4 µM FCCP. DatLab file from Hütter et al (2004), modified from Gnaiger (2020).

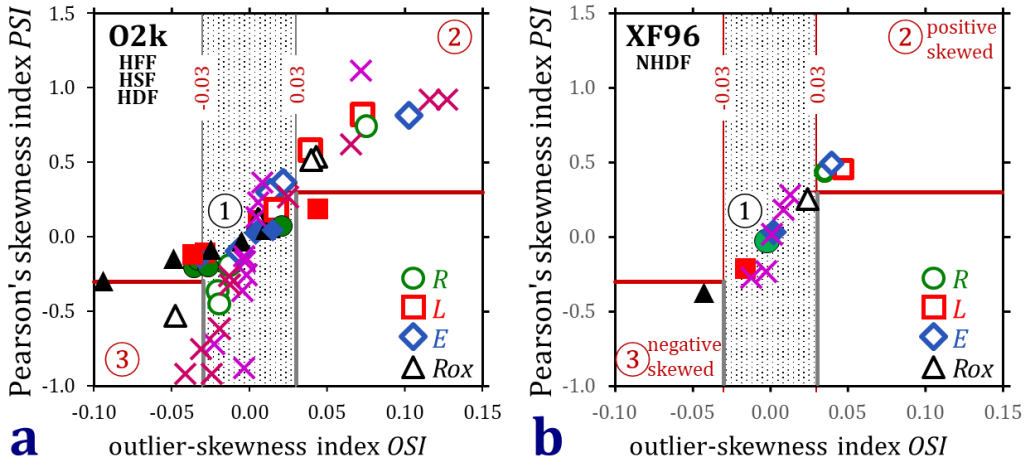

Figure 4. Relation between the Pearson 2 index *PSI* and the outlier-skewness index *OSI*. Area ①: Symmetrical data distribution with similar average $\bar{x}$ and median $\tilde{x}$ at $|OSI|<0.03$. Horizontal lines indicate $|PSI|<0.3$. ② Positive skewness, $\bar{x} > \tilde{x}$, suggesting log-transformation. ③ Negative skewness, $\bar{x} < \tilde{x}$. Open symbols and crosses: natural scale O_2 flow. Closed symbols: log-transformed O_2 flow. Crosses: flux ratios; most frequently symmetric without log-transformation. **(a)** HFF, HSF and HDF; LEAK *L* (open red squares) are more symmetric after log-transformation (full red squares). Crosses: only (*R*-*L*)/*E* in S-HFF (pink) and three ratios in HSF (dark red) are positive skewed. **(b)** NHDF; *R*, *L* and *E* are symmetric after log-transformation; open triangle (*Rox*) is negative skewed after log-transformation (closed triangle). Data from Tables 3 and 4.

3.2. Age- and senescence-related respiration in human fibroblasts

An age-related mitochondrial dysfunction in skin fibroblasts was linked to the decline in mitochondrial protein synthesis (Greco et al 2003). Fetal fibroblast samples are not included in the present meta-analyis. Fibroblast respiration expressed per cell shows a high variation throughout donor age (Figure 5a). Surprisingly, the variability is not reduced by normalization of respiration for protein mass per cell (Figure 5b). Protein mass per cell as an estimate of cell size shows an increasing scatter at age >50 y, which provides a rationale for splitting the data set into different age groups (Figure 5c). Although the coupling efficiency $j_{E\text{-}L}$ and *R*-*L* control efficiency $j_{R\text{-}L}$ are independent of normalization by protein mass, the scatter increases towards lower values at older age (Figure 5d). The *E*-*R* reserve efficiency $j_{E\text{-}R}$ is independent of age (not shown).

Although age group A-HSF (59-103 y) extends to larger cell size, plots of LEAK respiration per cell as a function of protein mass per cell are homolinear (Figure 1). ROUTINE respiration and ET capacity per cell, however, show a trend towards diminished increase with cell size in the age group A-HSF (59-103 y) compared to Y-HSF (1-42 y), suggesting two heterolinear clusters with large overlap (Figure 6a and b). The lower slope reduces the coupling efficiency $j_{E\text{-}L} = 1\text{-}L/E$ at older age by a diminished increase of *E* with increasing *L* relative to the young donors. The ratio of proportional slopes for *R* and *E* provides an estimate of the *R*/*E* flux control ratio, which is 100/174 = 0.58 and 71/91 = 0.78 for Y- and A-HSF, respectively. Both values are lower than the

medians or averages calculated from the individual R/E ratios (Table 4). However, the E-L coupling efficiencies calculated from the mean proportional slopes (Figure 1e and 6b) correspond to $\tilde{x}$ and $\bar{x}$ of the individual coupling efficiencies, at j_Y = 1-16.5/174 = 0.90 and j_A = 1-16.5/91 = 0.82, for Y- and A-HSF, respectively (compare Table 4). The relevant questions are (*1*) the reproducibility of discriminating separate clusters and (*2*) the accuracy of the estimate of a ratio or slope.

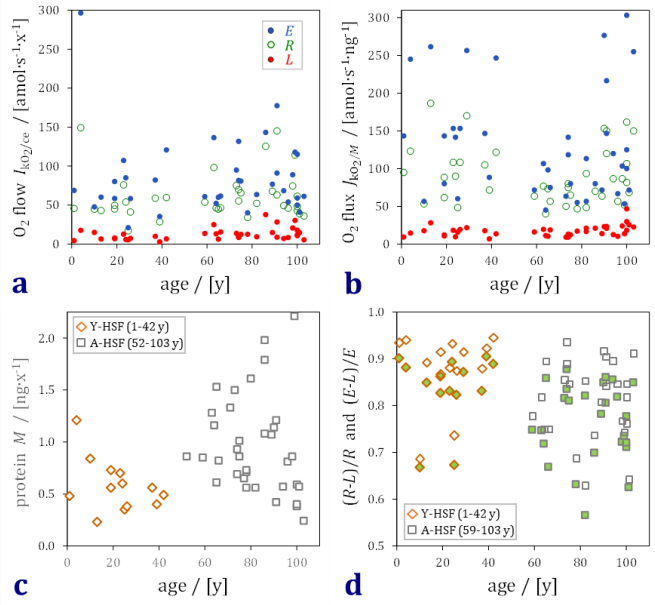

Figure 5. Human skin fibroblasts studied over the human donor age (based on data from Greco et al 2003). (a) O_2 flow per cell; **(b)** O_2 flux per protein mass of the cell as a function of donor age. Rates R in the ROUTINE state, L in the oligomycin-inhibited LEAK state, and E in the uncoupler-stimulated ET state. Neither representation reveals conclusive information on the effect of donor age on mitochondrial function. **(c)** Protein mass per cell. **(d)** E-L coupling efficiency $j_{E\text{-}L}$ (open symbols) and R-L control efficiency $j_{R\text{-}L}$ (closed symbols) as a function of age; the scatter increases in A-HSF.

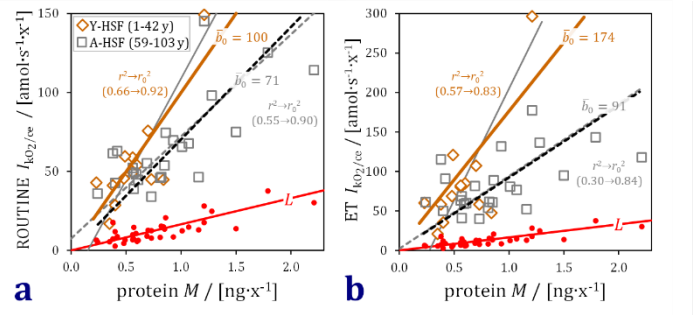

Figure 6. ROUTINE respiration (a) and ET capacity (b) as a function of cell size. LEAK respiration L (red line, full circles) inserted as a reference from Figure 1e. Y-HSF (full lines); A-HSF (dashed lines). Mean slopes of inverted linear least squares regression (thin regression lines extrapolated to zero) or proportional regression (through the origin; $\bar{b}_0$).

Young and aged HSF do not show separate clusters in plots of ROUTINE respiration/ET capacity (Figure 7a*R*). Although flux control ratios and control efficiencies are independent of normalization of O_2 flow or O_2 flux — the same ratio is obtained for I_{O2}(state *i*)/I_{O2}(reference state) and J_{O2}(state *i*)/J_{O2}(reference state) (Eq. 1) —, the ranges of flows and fluxes change and the slope between the two states depends on the normalization. The dimensionless O_2 consumption rate expressed per median ET capacity normalized for cell size (HSF; Figure 7c) reduces the range by 30 % compared to rates relative to the median ET capacity normalized for cell count (HSF; Figure 7b).

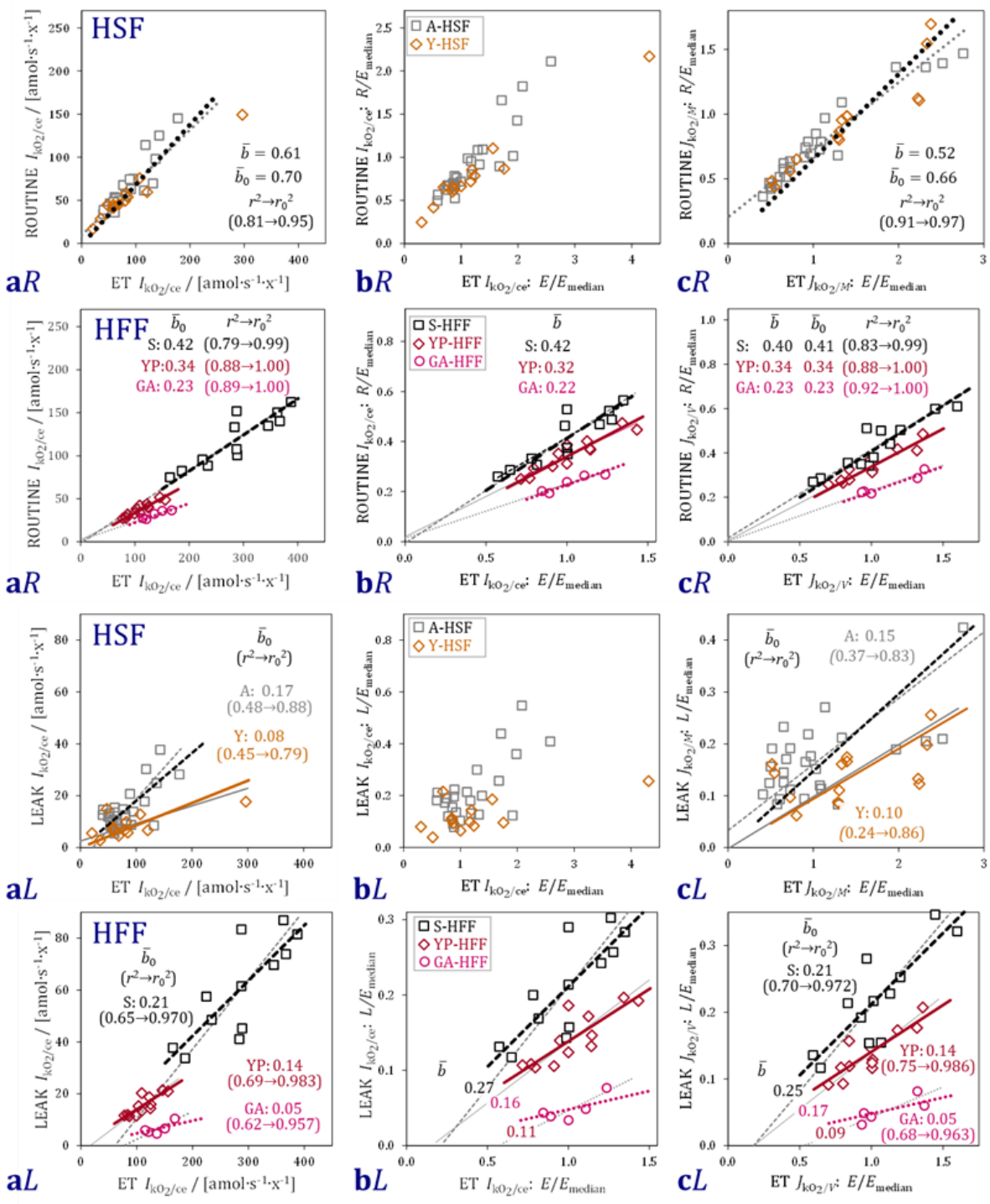

Figure 7. Respiratory control in human skin fibroblasts HSF (based on data from Greco et al 2003) and foreskin fibroblasts HFF (based on data from Hütter et al 2004). Mean slopes of inverted least squares linear regressions ($\bar{b}$; thin regression lines extrapolated to zero) or proportional regressions (through the origin; $\bar{b}_0$; short regression lines). Numbers are slopes; numbers in parenthesis are linear or proportional r^2. Y-HSF (full lines); A-HSF (dashed lines). YP-HFF (full lines); GA-HFF

(dotted lines); S-HFF (dashed lines). **(a)** O_2 flow expressed per cell count [amol·s^{-1}·x^{-1}]. Identical axes within **a***R* and within **a***L* for direct comparison. The clusters of HFF indicate mainly the effect of the larger cell size of senescent cells S-HFF on O_2 flow. **(b)** Dimensionless O_2 rate expressed per median ET capacity expressed per cell, resulting in identical slopes as in panels **a**. For HSF the data distribution is identical as in panel **a**, since the common median for both age groups is used (the medians for each group are not different; Table 3). **(c)** Dimensionless O_2 rate expressed per median ET capacity normalized for cell size. **(***R***)** ROUTINE respiration and ET capacity; axes ratios y/x fixed at 0.60. Age groups (HSF) do not show separate clusters in *R* and are combined in a single regression (dotted lines) indicating a possible nonlinearity, with a steeper slope from zero to low rates. **(***L***)** LEAK respiration and ET capacity; axes ratios y/x fixed at 0.20.

Proliferating cells growing exponentially represent the standard cell culture conditions in many studies. Proliferating human foreskin fibroblasts (YP-HFF) have a cell volume of 2.6 ± 0.3 pL·x^{-1} and are compared to senescent cells (S-HFF) which stop dividing and increase in volume per cell to 9.9 ± 0.9 pL·x^{-1}, whereas growth-arrested cells GA-HFF have a cell volume of 2.2 ± 0.2 pL·x^{-1} (Hütter et al 2004). In a plot of ROUTINE respiration/ET capacity per cell, the small YP-HFF and large S-HFF form two apparently isolinear clusters on a common trend of *R* increasing with *E* (HFF; Figure 7a). Normalization by the median ET capacity of each cell type shifts their rates to comparable scales and reveals the heterolinearity of the clusters (HFF; Figure 7b). Normalization for cell volume has the same effect on representing the three cell types as heterolinear bioenergetic clusters (HFF; Figure 7c). The pattern of higher LEAK respiration in the senescent HFF and aged HSF cells is comparable (Figure 7*L*). Higher *L*, however, causes an increase of ROUTINE respiration indicative of uncoupling or dyscoupling in HFF, in contrast to the conserved *R*/*E* slope in A- and Y-HSF (Figure 7*R*).

The proportional slopes $\bar{b}_0$ between ROUTINE respiration and ET capacity (HFF; Figure 7*R*) are identical to the median of the *R*/*E* flux control ratio of 0.34 (mean 0.34 ± 0.02 SD; Table 4) and 0.42 (mean 0.42 ± 0.05 SD) in YP-HFF and S-HFF, respectively. While the intercepts in the *R*/*E* plots are not different from zero, the corresponding *L*/*E* plots show a trend to negative intercepts and, therefore, for *L* to decline to zero at low *E* (HFF; Figure 7b*L* and c*L*). The same trend is seen in two separate studies of human dermal fibroblasts (Figure 8).

3.3. Outlier identification by bioenergetic cluster analysis

HFF were studied with the 2-mL chambers of the O2k, whereas the 0.5-mL module was used for neonatal HDF (Tables 3 and 4) to reduce the number of cells required for respirometric measurements and comparison with parallel measurements in the Seahorse XF24 (Zdrazilova et al 2021). Neonatal NHDF cells are controls for fibroblasts from patients suspected of mitochondrial diseases, studied with the XF96 (Yépez et al 2018). Respiration of NHDF and HDF measured in two different platforms are superimposed in Figure 8. No outliers are detected in the HDF study with the O2k.

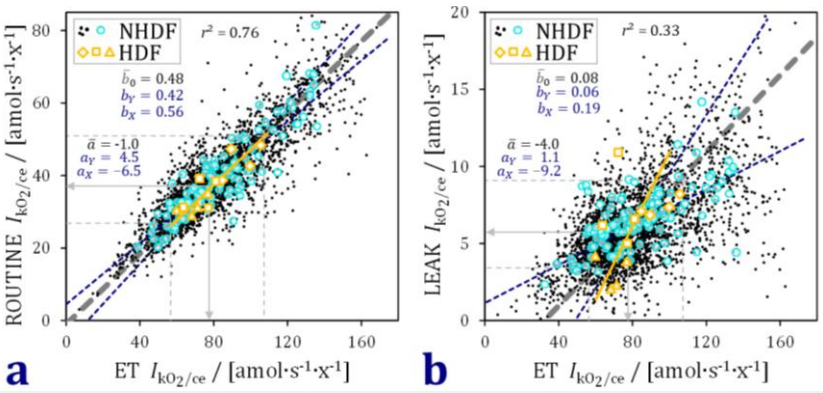

Figure 8. NHDF and HDF fibroblast respiration in relation to electron transfer (ET) capacity. Normalization for seed cell count. Meta-analysis of raw data from Yépez et al (2018) measured in the XF96. *n*=2630 wells after elimination of 6.8 % outliers. Dashed lines are mean inverted linear regressions $\bar{b}$, b_Y and b_X. $\bar{b}_0$ is the mean proportional slope. Open circles: averages within plates (*N*=124, median 20 wells per plate). Superimposed data from Zdrazilova et al (2021) on three HDF cell lines (yellow diamonds, squares and triangles) measured in the 0.5 mL-volume O2k with four repeats each. Full yellow lines are mean inverted linear regressions. **(a)** ROUTINE flow baseline-corrected for *Rox* as a function of *E*. Regression intercepts are not different from zero. **(b)** LEAK flow baseline-corrected for *Rox* as a function of *E*. NHDF: (min|L1, L2, L3|); averages (arrows) ± SD (dashed lines) calculated from log-transformed data. The proportional slopes $\bar{b}_0$ represent the *R*/*E* and *L*/*E* flux control ratios (compare Table 4).

The definition of outliers exerts a strong influence even on large data sets, must be considered carefully and be reported explicitly. Outlier identification provides a benchmark for BCA with transparent and traceable characterization beyond mere detection. Assays with missing data points (<3 measurements per respiratory state) are excluded from the present meta-analysis, which then contains *n*=2822 assays on NHDF.

Plots of ROUTINE respiration *R* as a function of ET capacity *E* show the time course of BCA from R1 to R3 (Figure 9R). At time periods R2 and R3 a distinct bioenergetic cluster *R*C2 appears of collapsed *R* (Figure 9R). Since R3 is used (Figure 3c), outlier cluster *R*C2 must be eliminated (BCA outlier level 3; see below). Inhibition of respiration by oligomycin occurs rapidly from R3 to L1. Two clusters are apparent in L1, with high *L* at low *E* in *L*C2. Cluster *L*C3 with even higher *L* crops up in L2 and L3. The minimum O_2 flow from L1 to L3 is used in the analysis, which eliminates the high LEAK rates of *L*C3 (Figure 9L). ET capacity drops to zero in cluster *E*C2 appearing in E2 and E3 (Figure 9E). In contrast to selecting minimum values for LEAK and residual baseline states, the maximum measured ET capacity is selected. This eliminates the low-ET capacity cluster *E*C2. Edge effects do not remove the outlier clusters (excluding all rows A and H, and all columns 1 and 12 of the 96 well plate).

Physiological outlier level 1: Exclusion of one negative *E*-*R*, one negative *R*-*L*, and — after baseline correction for *Rox* — seven negative *L*.

BCA outlier level 2: Two heterolinear clusters *L*C1 and *L*C2 in the *L*/*E* plot (Figure 10a) indicate that the *L*/*E* flux control ratio and *E*-*L* coupling efficiency (Eq. 4) differ in these clusters. Therefore, the cluster *L*C2 can be separated as *l*C2 by a threshold of low coupling efficiency, excluding 62 data with (*E*-*L*)/*E* < 0.8 (Figure 10b). In contrast, a plot of *E*-*L* coupling efficiency over *L* fails to discriminate separate clusters (Figure 10c).

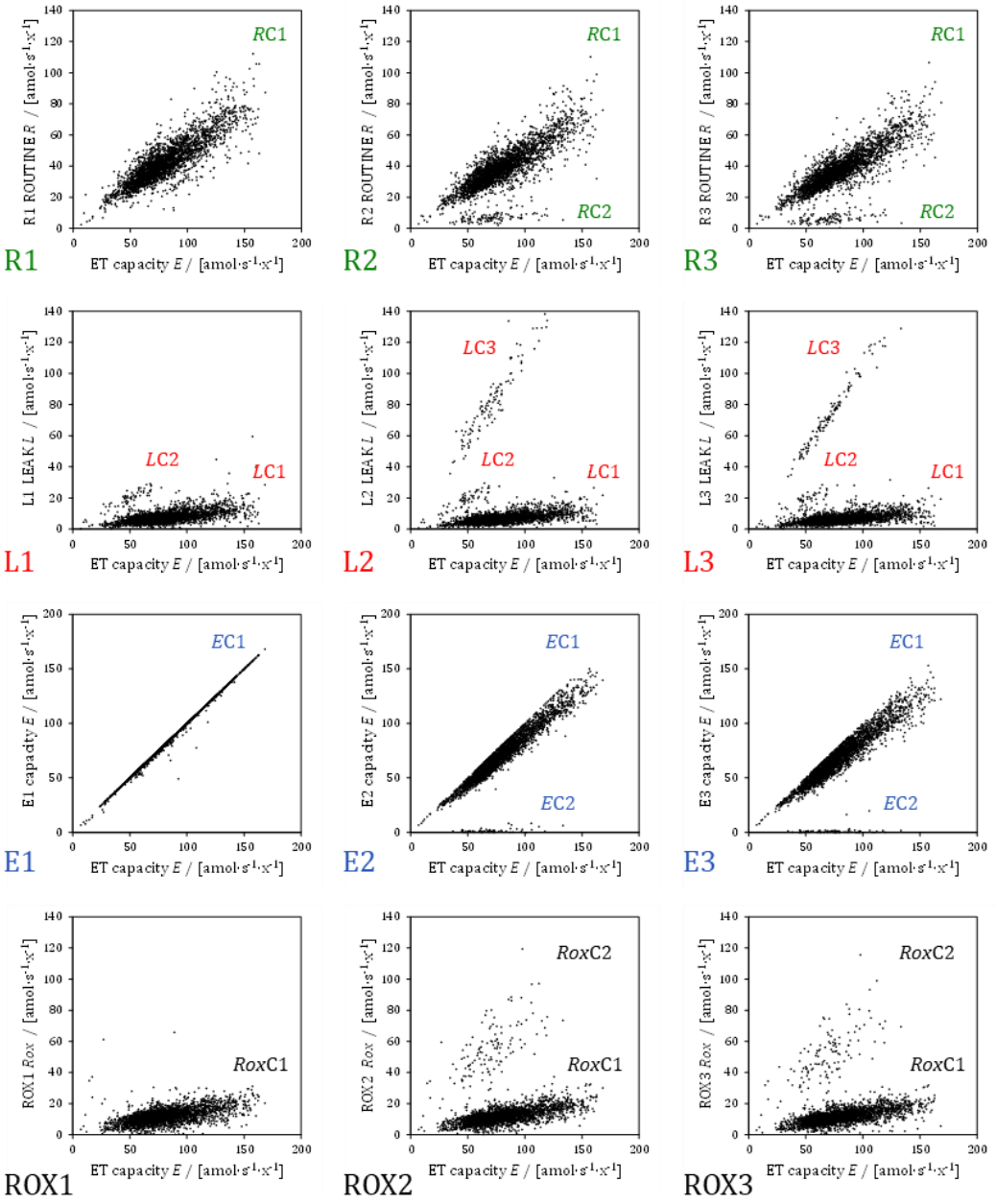

Figure 9. Three consecutive time intervals of ROUTINE respiration (R1-R3), LEAK respiration (L1-L3), ET capacity (E1-E3), and baseline (ROX1-ROX3) as a function of maximum ET capacity in NHDF cells measured in the XF96. Raw data from Yépez et al (2018) normalized for the seed cell count and baseline-corrected for *Rox*. A bioenergetic cluster *RC2* of low *R* appears in R2 and R3, arguing for using R1 instead of R3. A cluster *LC2* of intermediate *L* in L2 and L3 is apparent in L1, which is not eliminated by selecting minimum values of *L*. Clusters of high *L* (*LC3*) and *Rox* (*Rox*C2) appear at time intervals 2 and 3, which are eliminated by using minimum values of *L* and *Rox*. The maximum ET capacity *E* is almost exclusively obtained in E1. *EC2* with collapsed ET capacity appears in E2 and E3.

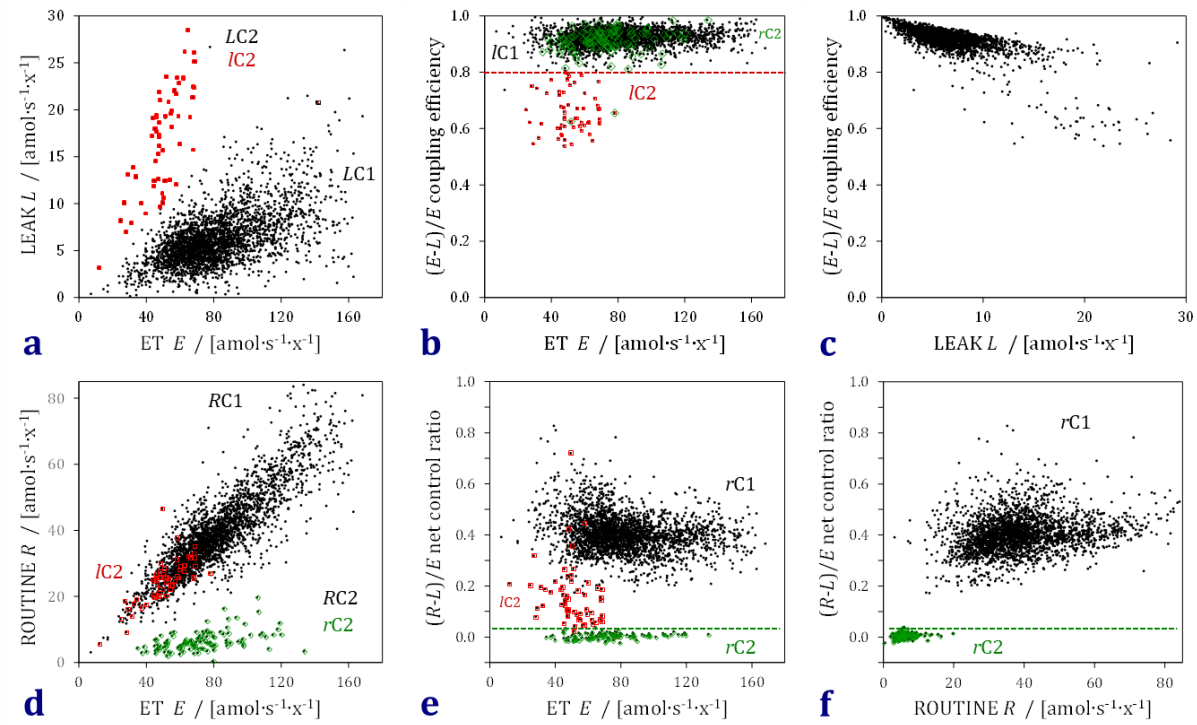

Figure 10. Bioenergetic cluster analysis for identification of outliers. Clusters *R*C and *L*C within time intervals (Figure 9) remain as clusters *r*C and *l*C after selection of time intervals. **(a)** *L*/*E* plot: heterolinear bioenergetic cluster *L*C2 with high *L*/*E* flux control ratio (Figure 9L) remains after selection of *L* = min|L1, L2, L3|. The cluster *l*C2 from panel **b** is superimposed as red squares. **(b)** Cluster separation: dispersed bioenergetic cluster *l*C2 with low coupling efficiency threshold (*E*-*L*)/*E* < 0.8 is associated with low ET capacity. The core cluster *l*C1 indicates that *E*-*L* coupling efficiency remains constant over the large range of *E*, reflecting the proportional variation of *L* and *E* (panel **a**). **(c)** The plot of coupling efficiency as a function of LEAK respiration does not allow for cluster separation but indicates increased *L* in addition to lower *E* as causes for the low-efficiency cluster *l*C2 in panel **b**. **(d)** *R*/*E* plot: heterolinear bioenergetic cluster *R*C2 with low *R*/*E* flux control ratio (compare Figure 9R). The *l*C2 cluster (red squares) is indistinguishable from the core cluster *R*C1. The cluster *r*C2 from panel **e** is superimposed as green diamonds. **(e)** Cluster separation: dispersed bioenergetic cluster *r*C2 with a threshold at low net *R*/*E* control ratio (*R*-*L*)/*E* < 0.04, separate from the bulk data but distributed across ET capacities. Cluster *l*C2 from panel **b** is superimposed as red squares, separating *r*C1 and *r*C2 even more distinctly. In contrast, the *r*C2 cluster (green diamonds) is indistinguishable from *l*C1 in panel **b**. Only two data points overlap in the *r*C2 and *l*C2 cluster. **(f)** The plot of net *R*-*L* control ratio over *R* reveals that low *R* independent of variation in *E* causes the low *R*-*L* control ratio in cluster *r*C2. Taken together, (*R*-*L*)/*E* < 0.2 is eliminated (except for three data points) by these two outlier clusters.

BCA outlier level 3: Whereas R1 avoids the cluster *R*C2 (Figure 9R), selecting R1 as the indicator of ROUTINE respiration would neglect the gradual decline of *R* in R2 and

R3 (Figure 3c). R3 is used in line with the original publication. The heterolinear cluster *R*C2 in the *R*/*E* plot (Figure 10d) can be separated as *r*C2 by (*R*-*L*)/*E* < 0.04 with 115 outliers (Figure 10e). Elimination of *r*C2 removes the spurious clusters *R*C2, *L*C3, *E*C2, and *Rox*C2 (Figure 9). This outlier cluster lacks any scope for aerobic ATP production — with collapsed net ROUTINE respiration *R*-*L* (*r*C2 in Figure 10f) — but shows a normal range of ET capacities measured subsequently in the coupling control protocol (Figure 9E1 and 10e). Only two data points belong to both outlier clusters *l*C2 and *r*C2, hence 175 data are eliminated for *l*C2 and *r*C2. *l*C2 is linked only to *L*C2 (Figure 9L).

Statistical outlier level 4: For the average ± 5·SD_{ln}, all lower boundaries were below zero, and the upper boundaries were 98.4, 19.9 and 207 for *R*, *L*, and *E*, respectively, excluding 8 outliers (4 for *R*; 4 for *L*; 0 for *E*). This results in a total of 6.8 % outliers out of 2822 data, with *n*=2630 data remaining for final analysis as presented in Figure 8.

3.4. Low coupling efficiency: dyscoupling and dyscapacity

The drivers of ROUTINE respiration are (*1*) the demand for coupled energy transformation in OXPHOS and (*2*) uncoupling or dyscoupling. Uncoupler titrations initiated in the ROUTINE state stimulate respiration progressively. Similarly, ROUTINE respiration is increased by intrinsic physiological uncoupling or pathological dyscoupling if LEAK respiration is increased at constant ET capacity. This is the case in senescent cells (dyscoupling), which have lower *E*-*L* coupling efficiencies compared to young proliferating and growth-arrested fibroblasts, as discussed by Hütter et al (2004) (HFF; higher *L*/*E* slope in Figure 7*L*).

The coupling efficiency (*E*-*L*)/*E* (Eq. 4) declines due to (*1*) *increasing* LEAK respiration at constant *E*, or (*2*) *decreasing* ET capacity relative to *L*. These dysfunctions are linked to different OXPHOS modules and are distinguished as *dyscoupling* at reduced phosphorylation (transmembrane proton leak and slip) at a given O_2 consumption rate, and *dyscapacity* at reduced oxidation (enzymatic defects of the electron transfer system). Relationships between the components of the *E*-*L* coupling efficiency and their effects on ROUTINE respiration are outlined in the bioenergetic cluster analysis of living cells:

(**a**) ROUTINE respiration increases linearly as a function of LEAK respiration in all fibroblast cell lines, but with different *R*/*L* slopes and intercepts >0 (Figure 11.a). HFF form isolinear clusters (Figure 11.a2). S-HFF are not only more dyscoupled compared to young cells — as seen by increased LEAK respiration relative to E_{median} — but compensate the lower coupling efficiency by the proportionally increased ROUTINE respiration, thus dissipating more energy to maintain a constant net*R*/*E* control ratio (*R*-*L*)/*E*. This is the mechanistic interpretation of overlapping homolinear clusters, where rates increase on a common regression line from young growth-arrested GA-, to young proliferating YP-, and senescent S-HFF cells (Figure 11.a2).

(**b**) The difference *R*-*L* is the net ROUTINE capacity net*R* (vertical arrows in Figure 11.a), which is the physiological rate of electron transfer potentially coupled to ATP production. net*R* increases proportionally with *E* (Figure 11.b). The proportional slope $\bar{b}_0$ and slopes b_Y and b_X can be compared with the $\tilde{x}$±SD ranges of (*R*-*L*)/*E* in Table 4.

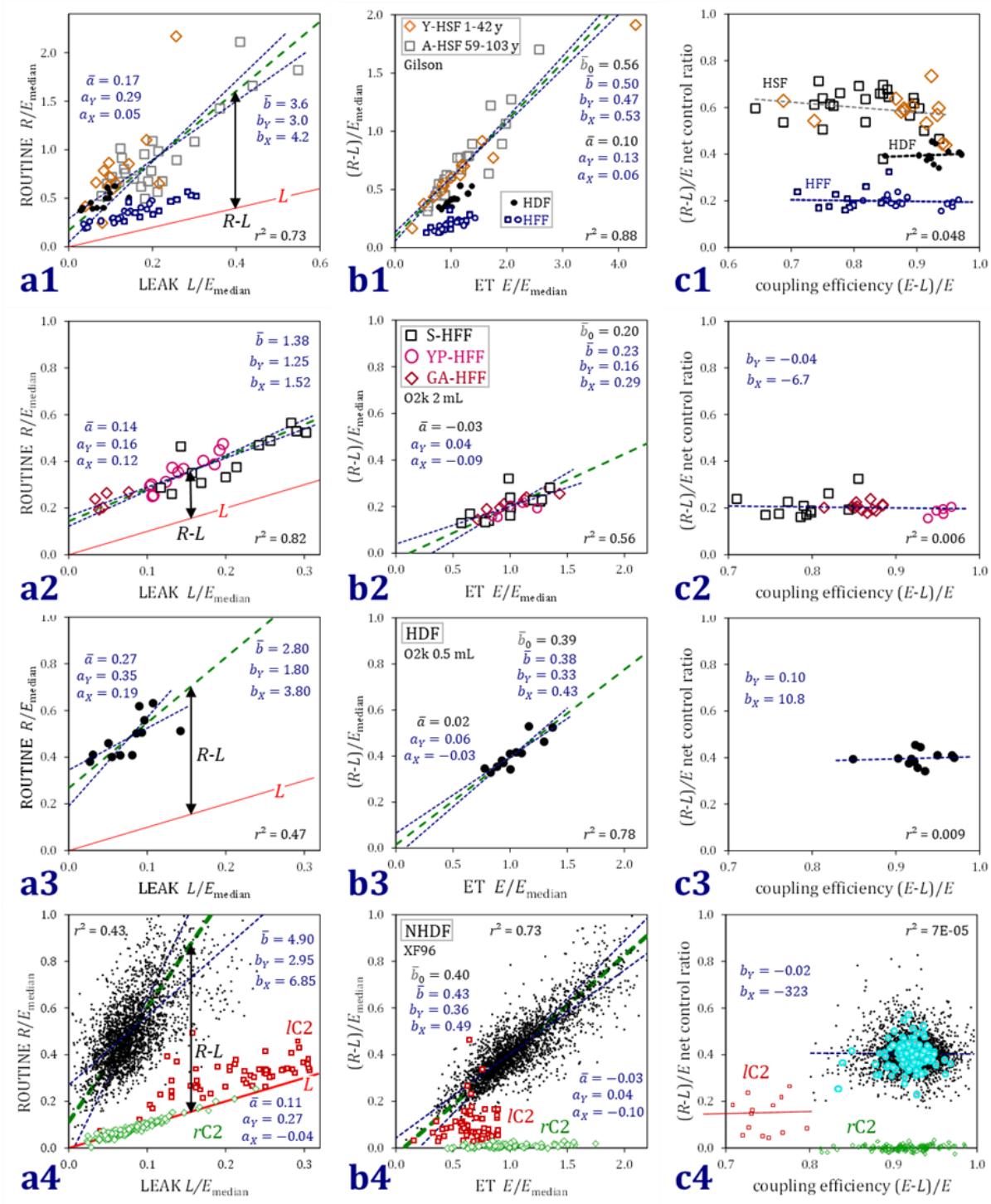

Figure 11. Bioenergetic cluster analysis: compensatory control of ROUTINE respiration *R* by LEAK respiration *L* maintaining a constant *R-L* net control ratio at declining coupling efficiency. (a) Linear increase of *R* as a function of *L*, normalized for E_{median} (O_2 flow per cell). Positive intercepts of *R* at zero *L*. Vertical arrows indicate the difference *R-L*. **(b)** Proportional increase of net ROUTINE capacity *R-L* as a function of *E*, normalized for E_{median} (O_2 flow per cell). Subtraction of *L* from *R* yields net

ROUTINE respiration which is available for ATP production. The proportional slopes $\bar{b}_0$ are comparable with the means of (*R-L*)/*E* (Table 4). **(c)** Constant (*R-L*)/*E* net control ratio independent of *E-L* coupling efficiency. (*R-L*)/*E* remains constant and independent of coupling efficiency, when dyscoupling or uncoupling is compensated for by stimulation of ROUTINE respiration at constant *E*, or when *R-L* decline proportionally with diminished ET capacity at constant *L*. **(1)** Aging and human skin fibroblasts (HSF; Gilson 1.5-mL chamber; Greco et al 2003). For comparison, data points for HFF and HDF are superimposed from panels **2** and **3** since scales are different in panel **1** from panels **2** to **4**. **(2)** Senescent (S), young proliferating (YP), and young growth-arrested (GA) human foreskin fibroblasts (HFF; O2k 2 mL-chamber; Hütter et al 2004). Normalization for E_{median} in each cell type. **(3)** Human dermal fibroblasts (HDF; O2k 0.5 mL-chamber; Zdrazilova et al 2021). **(4)** Normal human dermal fibroblasts (NHDF, XF96; Yépez et al 2018). Black dots and circles: individual wells and averages within plates without outliers. Outlier clusters *l*C2 ($j_{E\text{-}L}$ declines to 0.53) and *r*C2 as defined in Figures 10b and e, respectively. In panel **a4**, the slope and intercept are 1.04 and 0.00 in *r*C2, therefore *R*~*L*. Normalization for E_{median} in the total data set, since clusters *l*C2 and *r*C2 are separated by BCA *a posteriori*.

(**c**) A proportional dependence of *netR* on *E* implies that the net control ratio (*R-L*)/*E* is regulated at a narrow level despite of variable *E-L* coupling efficiency (Figure 11.c). Comparison of neonatal HDF (O2k) and NHDF (XF96) control groups indicates a similar narrow range of coupling efficiency, but high noise in the net control ratio (*R-L*)/*E* of NHDF (Figure 11.c3 and 11.c4). In another O2k study, the coupling efficiency varies between 0.90 and 0.97 in human dermal fibroblasts from young to old people, whereas the respiratory net control ratio (*R-L*)/*E* is constant in the narrow range from 0.23 to 0.26 (calculated from Kozieł et al 2011). A wide scatter on both axes may indicate instrumental noise (Figure 11.c4).

Respiratory capacity per cell changes at constant mitochondrial quality as a function of mitochondrial content per cell, reflected by constant flux control ratios and *E-L* coupling efficiency. In the coupling control protocol of living cells, ET capacity is the most difficult attribute to be measured accurately. Independent of *R* and *L*, *E* may be underestimated due to inhibition of *E* by oligomycin (Doerrier et al 2018) or failure to titrate optimal uncoupler concentrations (Steinlechner et al 1996; Gnaiger 2008). Then the coupling efficiency $j_{E\text{-}L}$ declines at constant *L* (Zdrazilova et al 2021). Variation of *E* and *netE* = *E-L* independent of *L* results in a hyperbolic function of $j_{E\text{-}L} = netE/E$ in the dyscapacity model (Figure 12a),

$$j_{E-L} = \frac{j_{netE\max} \cdot netE}{netE_{50} + netE} \qquad \text{Eq. 15}$$

where the maximum coupling efficiency $j_{netE\max}$ equals 1 by definition. The decline of $j_{E\text{-}L}$ to 0.5 is defined by $netE_{50} = L$ as required in Eq. 15 ($netE_{50}+netE = E$) to satisfy Eq. 4. Artificially low values of *E* are detected as physiological outliers if *R*<*E*. The continuous pattern of such physiological HSF outliers in the total HSF data set suggests that the lower coupling efficiency in fibroblasts from aged donors (Table 4) is not due to dyscoupling but is rather caused by declining *E* relative to a more stable *L* according to

the hyperbolic dyscapacity model (Figure 12b). This conclusion is supported by the isolinear dependence of L on protein mass per cell in A-HSF and Y-HSF (Figure 1) as opposed to the lower slopes of R and E in A-HSF than Y-HSF (Figure 6). In contrast, coupling efficiencies $j_{E\text{-}L}$ differ between young and senescent HFF according to the dyscoupling model (Figure 12c). However, $j_{E\text{-}L}$ is constant in each cell type despite of variation of ET capacity, suggesting that although mitochondrial quality differs between cell types with different $j_{E\text{-}L}$, it is maintained in each cell type when mitochondrial contents change (preserved mt-quality model; Figure 12c).

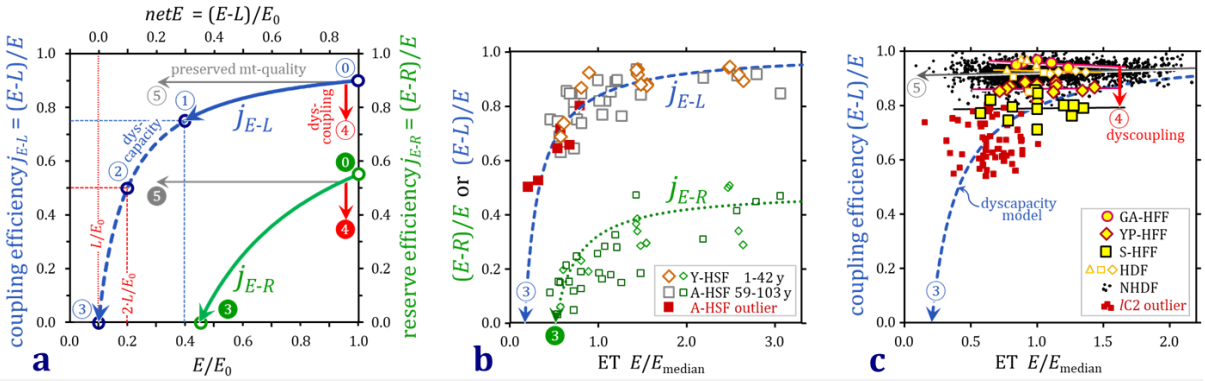

Figure 12. Coupling and reserve efficiency at varying ET capacity. (a) Models: ⓪ Reference state at zero inhibition of $E = E_0$; $(E\text{-}L)/E = 0.9$; ⓪ $(E\text{-}R)/E = 0.55$. ⓪→③ and ⓪→③ ET dyscapacity: decline of E and R at constant L. Hyperbolic dependence of $j_{E\text{-}L}$ on $netE$ and $j_{E\text{-}R}$ on $netR=(E\text{-}R)/E_0$. ⓪→① Coupling efficiency is insensitive to inhibition of E, declining from 0.9 to 0.75 when E is inhibited by 60 % to $E/E_0 = 0.4$. ② Decline of $j_{E\text{-}L}$ by 50 % at $E/E_0 = 2{\cdot}L/E_0$. ③ and ③ Zero coupling and reserve efficiency at the threshold $E/E_0 = L/E_0$ and $E/E_0 = R/E_0$, respectively. Negative efficiencies are artificial physiological outliers. ④ and ④ Dyscoupling: increasing L and declining coupling and reserve efficiency at constant E. ⑤ and ⑤ Preserved mt-quality: constant coupling and reserve efficiency at proportional decline of E, L and R due to lower mt-content per cell. **(b)** HSF: hyperbolic fit (excluding 6 physiological outliers with $E\text{-}R < 0$; full red squares) in line with the dyscapacity model with declining E at constant L. An inhibitory effect on E by the high oligomycin concentration cannot be excluded. The mean L/E_{median} is 0.17 as estimate of $E/E_0 = L/E_0$ ③ in agreement with the hyperbolic fit. $j_{E\text{-}R}$ does not follow the dyscapacity model. Asymmetry of experimental artefacts results in underestimation but not overestimation of E, which causes low apparent ET capacity even above the physiological outlier detection limit ③; variability of high ET at constant mitochondrial quality leads to a plateau of $j_{E\text{-}R}$. **(c)** HFF and HDF (open symbols) and NHDF (dots): different coupling efficiencies between cell lines (dyscoupling model ④) but independence of $j_{E\text{-}L}$ within cell lines at variable E expressed relative to the median E for each cell line. Horizontal linear regressions indicate a proportional change of L and E at variable mitochondrial content in line with the preserved mt-quality model ⑤, supported by constant $j_{E\text{-}R}$ within each cell line (not shown). The alternative hyperbolic dyscapacity model (dashed line) fitted through the BCA outlier cluster *l*C2 (Figure 11.4) with variable underestimation of E when L remains constant at 0.21 according to the hyperbolic fit. The mean L/E_{median} is 0.22 ③ for the data in the outlier cluster *l*C2.

Outlier cluster *l*C2 in NHDF is identified by BCA at low ET capacity (Figure 10b) and conforms to the dyscapacity model (Figure 12c). Coupling efficiencies are identical in HDF and NHDF (Figure 12c; excluding outliers). When coupling efficiency is maintained in a narrow range (Figure 11.c3 and c4), all respiratory states in the coupling control protocol vary in direct proportion (constant quality model). Then variability of O_2 flow per cell may be caused by physiological variations of mitochondrial content per cell due to (*1*) different cell size and (*2*) different mt-densities. Experimental and instrumental causes are errors in (*3*) cell counting; (*4*) titration of cells into the respirometric chamber; (*5*) volume calibration of the experimental chambers; and (*6*) estimation of variable fractions of cells outside of the closed configuration of a well.

4. Discussion

Respiratory control in human fibroblasts is compared quantitatively in a meta-analysis of data published by four different laboratories using four different respirometric designs. All results are expressed in SI units (Gnaiger et al 2020). Normalization of oxygen consumption rates as O_2 flow per cell has limitations particularly when cell size is variable. But cell count is the only common denominator across these studies.

Direct comparability of different cell cultures is limited if there are differences in (*1*) the sources and sizes of cells, (*2*) culture media and culture conditions, (*3*) passage number after thaw and confluence state before harvesting, (*4*) respirometric platforms with suspended or adherent cells, (*5*) incubation conditions and titration regimes, and (*6*) cell counters (Tables 3 and 4; Figure 3). Fibroblast respiration using commercially available control cells (HDF and NHDF) measured in the O2k with 0.5-mL chamber volume (Zdrazilova et al 2021) and XF96 (Yépez et al 2018) are comparable (Figure 8) based on (*1*) a carefully designed statistical experimental regime and explicit outlier detection strategies, (*2*) optimization of oligomycin and uncoupler concentrations by multiple titrations or separate control experiments, (*3*) baseline correction for residual oxygen consumption, and (*4*) normalization and expression of results in standardized units. The two platforms follow different strategies: high-resolution HRR in a limited number of diffusion-tight chambers versus high throughput in multi-well plates with high background effects due to O_2 diffusion into semi-closed chambers. Yépez et al (2018) suggest 12 wells are required as technical repeats per experimental arm and recommend using three plates for a resolution of 10 to 15 % differences. The between-plate variability is higher than between-well variation on a single plate, hence a control group should be included on each plate. Background effects are measured in parallel in four calibration wells in the XF96, whereas instrumental background tests are performed without sample in each chamber of the O2k. With 7 % outliers (present XF96 re-analysis after elimination of incomplete data sets) to 17 % outliers (Yépez et al 2018; outliers are not addressed by Zhang et al 2021) and 12 repeats, 6 experimental groups and one control can be included in each plate. This compromises high throughput. HRR does not support high throughput. But HRR minimizes outliers and adds quality control and flexibility in terms of titration regimes in the O2k.

Several studies of cell respiration are limited by the low number of independent replica *N* and technical repeats *n*. The objective evaluation and reporting of outliers represent a hot topic in the reproducibility crisis (Ulrich, Miller 2020). Bioenergetic cluster analysis provides a concept-driven graphical approach, which visualizes clusters of data based on bioenergetic functional relationships for the characterization of experimental groups (Figures 7, 8 and 11) or outliers (Figures 9 and 10). Compared to the debated terminology on *statistical significance* related to *p*-values (Amrhein et al 2019; Curran-Everett 2020), BCA expands the question about differences of data sets. Are clusters of data distributed along an identical linear or non-linear regression line of functional correspondence? Such *isolinear* clusters are separated by variations in the extent of a quantity that correlates with the rate (Figure 11a2). In contrast, *heterolinear* clusters fall on different regression lines (Figures 7 and 12c). This provides a necessary and sufficient proof of qualitative changes in the control of flux, such as dyscoupling that causes an increase of *L* (senescence) or dyscapacity that leads to low *E* and *R* (aging). *Dispersed* clusters are clouds of data separated by a critical threshold value, which may be achieved by selecting a specific normalization (Figure 10).

Hypothesis testing by conventional statistics refers frequently to the concept of *significance*. This paradigm is faced with the claim that '*inferences should be scientific, and that goes far beyond the merely statistical*' (Amrhein et al 2019). Integration of fundamental bioenergetic concepts into BCA (Gnaiger 2020) takes statistical analyses to a higher level of heuristics (Kahnemann 2011) for finding answers to scientific questions, compared to mere black-box dichotomization by frequentist or Bayesian statistics (Yépez et al 2018; Zhang et al 2021). Concept-driven normalization in BCA considers regression parameters within separate clusters. BCA-linked evaluation of the corresponding slopes and intercepts help in interpreting the linear functions (Figure 11). The slope of a proportional relationship through the origin represents the dimensionless flux control ratio. Figures 7a to c represent R/E and L/E plots. Variation of normalizations on the Y/X axes reveal bioenergetic clusters indicative of different features of mitochondrial respiratory control distinguishing these cell types. (**a**) O_2 flow per cell separates clusters with low and high O_2 flow due to the larger cell size in S-HFF. (**b**) O_2 consumption rates expressed per median ET capacity in each cell type shift the rates to numerically comparable scales and thus emphasize more visibly the heterolinear nature of the clusters and reveal uncoupling or dyscoupling of oxidative phosphorylation as the causes of different mechanisms of mt-respiratory control. Importantly, using the median respiratory capacity of the reference state on both axes does not depend on additional measurements of cell size, as shown by (**c**) comparison with normalization by cell volume or cell protein mass.

The variability of respiration in a cultured cell line is a dominant biological factor, superimposed by experimental errors. Respirometry and cell counting differ across laboratories. The variability introduced into respirometric results by the cell count is eliminated by (*1*) internal normalization as flux control ratios and flux control efficiencies, and (*2*) bioenergetic cluster analysis BCA with graphical representation of the relationship of O_2 consumption rates in respiratory states induced in the coupling control protocol. From the perspective of respirometry, *internal* normalization

eliminates errors of *external* attributes, such as cell count, cell protein mass, or marker enzyme activities. These provide specific additional information but may introduce more noise into respiratory data and increase biases between laboratories. By concept-driven internal normalization and regression analysis, higher resolution and greater information are gained on respiratory control patterns visualized by BCA. Taken together, BCA provides new insights into the interplay between diminishing electron transfer capacity and dyscoupling, which are in the numerator and denominator of *E*-*L* coupling efficiency. Complementary to conventional statistics, BCA reveals patterns of respiratory control in experimental or diagnostic groups. BCA is independent of respirometric methods and thus provides a general tool for evaluation of different instruments (Zdrazilova et al 2021).

5. Conclusions

1. Results on cell respiration are comparable only if experiments refer to accurately defined steady states. Rates should be stable over experimental periods of time in optimized respiration media supporting physiological fuel substrate supply to living cells preventing exhaustion of endogenous substrates. Concentrations of inhibitors and uncouplers must be titrated carefully to avoid inhibitory side effects, e.g. inhibition of ET capacity by oligomycin or by inadequate uncoupler concentrations.
2. Residual oxygen consumption *Rox* measured after inhibition of mitochondrial electron transfer may include chamber- or well-specific instrumental background effects. Corresponding baseline corrections of respiratory rates (*R*, *L*, *E*) eliminate such experimental artefacts.
3. Rates of cell respiration are expressed in generally accepted SI units and are normalized for cell count, cell size, or mitochondrial markers for comparability of results across projects, laboratories, and instrumental platforms. This encourages evaluation of replicability and extension of validated reference databases.
4. Normalization of respiratory rates for external markers adds valuable information. But normalization — e.g. by CS activity — may introduce noise into respiratory results, and bias particularly between laboratories.
5. Internal respiratory markers use O_2 consumption rates in a reference state for normalization. This yields flux control ratios *FCR* and flux control efficiencies *j* independent of any externally measured attributes of the sample. Then noise is typically lower. But the cost is entailed of reduced information compared with O_2 flow I_{O2} per cell and O_2 flux J_{O2} per cell size or per mt-elementary unit. An extension of the *FCR* concept is normalization by the median reference flux of a data set.
6. Irrespective of the chosen normalization, data obtained from SUIT protocols may be presented in conventional scatter plots where connections between data points are difficult to be shown. Rates measured in sequential respiratory states are connected within any single assay. Bioenergetic cluster analysis BCA represents selected data pairs as *Y*/*X* diagrams to identify functional relationships, e.g. between *L* and *R*. *Y*/*X* diagrams reveal clusters and data distribution more clearly than discriminatory statistical analyses. Proportional slopes through the origin are equivalent to *FCR*.

7. Ordinary regression analysis leads to a bias of underestimation of the slope and overestimation of the intercept if variables *Y* and *X* are measurements with error. Inverted regression analysis accounts for errors of variables on both axes. The coefficient of determination r^2 equals the slope ratio of inverted regressions.
8. The outlier-skewness index provides a guideline for outlier detection or characterization of asymmetrically distributed data sets. Positively skewed data should be log-transformed for calculation of SD and *p*-values.
9. A reasonable '*call for the entire concept of statistical significance to be abandoned*' (Amrhein et al 2019) should be considered. Therefore, asterisks and binary inequalities — $*p < 0.05$, $**p < 0.005$ — are eliminated. Clusters in BCA may appear objectively and convincingly, in which case *p*-values add no information.
10. BCA can be applied to small and large data sets for distinguishing isolinear, heterolinear and dispersed clusters. At the limit, however, a cluster of a large data set appears as a single but possibly unidentified outlier in a small data set. Physiological outliers — such as $E<R$ or $L<0$ — are recognized in any data set. Outlier clusters are identified by BCA in terms of specific dysfunctions, providing a basis for analyzing and finally minimizing the factors causing errors. Isolinear or heterolinear clusters indicate distinct mechanisms of mitochondrial dysfunction or metabolic reprogramming.

6. Methods

6.1. Human skin fibroblasts: HSF

Data were re-analyzed from Greco et al (2003), where the sources of cells and experimental conditions are described. The donor age spans from 1 to 103 years for mostly forearm or upper arm fibroblasts from cell repositories or biopsies. Respirometry was performed after two to three passages, trypsinizing exponentially growing cells, incubation at cell concentrations of $1.5 \cdot 10^6$ to $3 \cdot 10^6$ x/mL in Tris-based Mg^{2+}-Ca^{2+}-deficient medium (0.137 M NaCl, 5 mM KCl, 0.7 Na_2HPO_4, 25 mM Tris-HCl, pH 7.4), and respirometry in a 1.5-mL water-jacketed Gilson chamber using YSI polarographic oxygen sensors. Omy was used at a high concentration of 5 µg/mL (6.25 µM), which needs testing for inhibitory effects on ET capacity. The uncoupler dinitrophenol was titrated stepwise from 67-93 µM up to maximum O_2 consumption rates. ET was inhibited by 20 nM antimycin A (Greco et al 2003).

6.2. Human foreskin fibroblasts: HFF

Data were re-analyzed from Hütter et al (2004). Respirometric measurements were performed in 2.0-mL chambers of four O2k instruments (Oxygraph-2k; Oroboros Instruments, Innsbruck, Austria), with Dulbecco's modified Eagle's medium DMEM supplemented with penicillin/streptomycin and 10 % (v/v) fetal calf serum, containing substrates for cellular energy metabolism, such as glucose (5 mM), pyruvate (1 mM) and L-glutamine (4 mM). Pre-experiments in two to four chambers each of young proliferating human foreskin fibroblasts (YP-HFF; passage 13) and senescent cells (S-

HFF; passage 28) were not included in the experimental design. For each cell line, six O2k assays were performed in parallel chambers with cells obtained from separate culture plates, repeated on two different days several months apart (N = 2 independent replica; total n = 12 assays). No outliers were removed.

Young growth-arrested fibroblasts (GA-HFF; passage 13) were measured on a single day in six chambers, where one chamber was discarded due to formation of a gas bubble in the medium. Medians and means were not different (except for LEAK respiration in YP-HFF and GA-HFF with *OSI* of 0.039 and 0.073; the average |*OSI*| was 0.024 for *R*, *L*, and *E* in the three cell lines). Similarly, the average |*OSI*| was 0.017 for *R*/*E* flux control ratios, (*R*-*L*)/*E* and (*E*-*L*)/*E* control ratios. Thus log-transformation was not required.

The adjustment of the range in the axes of the plots in Figure 7 result in the graphical appearance of the variability of respiration relative to average or median O_2 flow. To remove the somewhat arbitrary scaling of the axes, respiration is divided by the median obtained in each respiratory state, and the relative O_2 fluxes are plotted at identical scales of 1.0 ± 0.6 in Figure 13. This illustrates quantitatively the dependence of the variability on the mean. The coefficient of variation (approximated as SD/mean) ranges from 0.20 to 0.31.

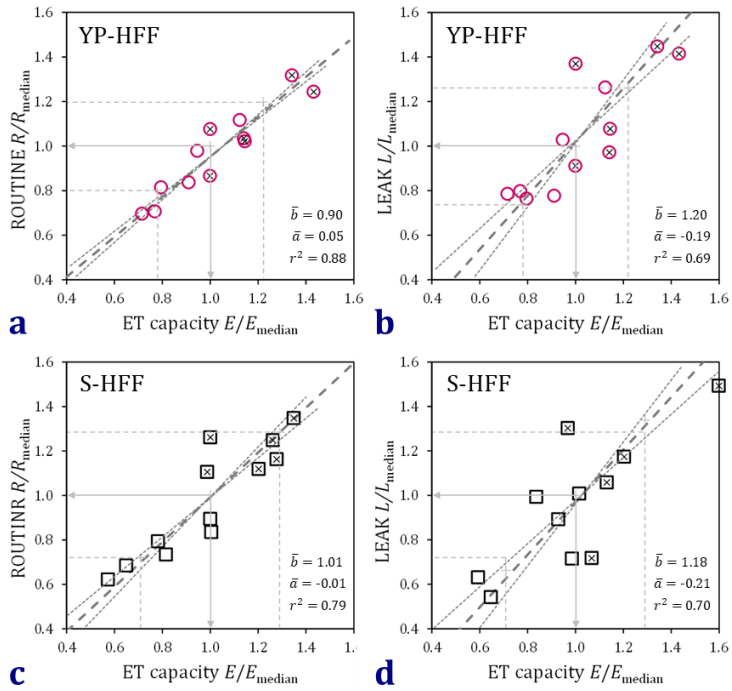

Figure 13. HFF fibroblast respiration in relation to electron transfer (ET) capacity. O_2 flow normalized for the median in each respiratory state. Symbols × indicate experiments on day 1, open symbols on day 2. Medians (arrows) ± SD (dashed lines; ±20 % to 30 %), at a range of ±40 % to ±60 %. (**a-b**) Young proliferating cells YP-HFF. (**c-d**) Senescent cells S-HFF. For further details, see Figure 7.

Residual oxygen consumption *Rox* tends to be lower on the first compared to the second experimental day by about 10 amol·s^{-1}·x^{-1} (not shown). Conversely, *Rox*-corrected O_2 flow (*R*, *L*, and *E*) shows a trend towards higher values on day 1. These differences are proportional and, therefore, are not explained by the relatively small additive effect of *Rox* correction but rather reflect cell physiology (Figure 13).

6.3. Human dermal fibroblasts: HDF and NHDF

Raw data on commercial cell lines of neonatal human dermal fibroblast HDF and one cell line from a nonmitochondrial patient at age of 5 months are available in (Zdrazilova et al 2021). Cells were cultivated in DMEM with 25 mM glucose and measured (passage 13 to 15) on three days in 0.5-mL O2k chambers with 375000 cells in DMEM (5 mM glucose, 2 mM pyruvate and 3.9 mM glutamate; Zdrazilova et al 2021).

Raw data on respiration of normal human dermal fibroblasts NHDF are listed in Yépez et al (2018). O_2 flow per well of the 96-well Seahorse XF96 Analyzer (Agilent, Santa Clara, USA) measured in bicarbonate-free DMEM is transformed into SI units [pmol·s^{-1}]. Flow per NHDF cell [amol·s^{-1}·x^{-1}] is normalized for seeded cell count of 20000 cells. In contrast to the continuous traces of respiration provided by DatLab (O2k software; Figure 3d), the Seahorse software restricts time resolution by calculating respiration at consecutive time intervals separated by reoxygenations. ROUTINE respiration declines over time towards a steady state at R3, whereas ET capacity becomes progressively inhibited after stimulation by a single dose of uncoupler (Figure 3c). This time dependence provides a physiological argument against the focus on the 'average behavior' of time intervals incorporated into the statistical analysis of Zhang et al (2021). Log-transformation is recommended for statistical evaluation due to skewed data distribution (Yépez et al 2018). Indeed, |*OSI*| averaged 0.043 for the natural values of *R*, *L*, and *E* before outlier removal, and was >0.035 for each state after outlier removal. Medians and standard deviations of data sets expressed on the natural and log-transformed scale are then compared after re-transformation to the natural scale. For the logarithmic transformed data and expression of μ and σ as $\bar{x}$ or $\tilde{x}$ and SD_{ln} on the natural scale (Eq. 14), the corresponding |*OSI*| was <0.03 (average 0.009). |*OSI*| was <0.02 (average 0.008) for *R*/*E*, (*R*-*L*)/*E*, and (*E*-*L*)/*E* without logarithmic transformation.

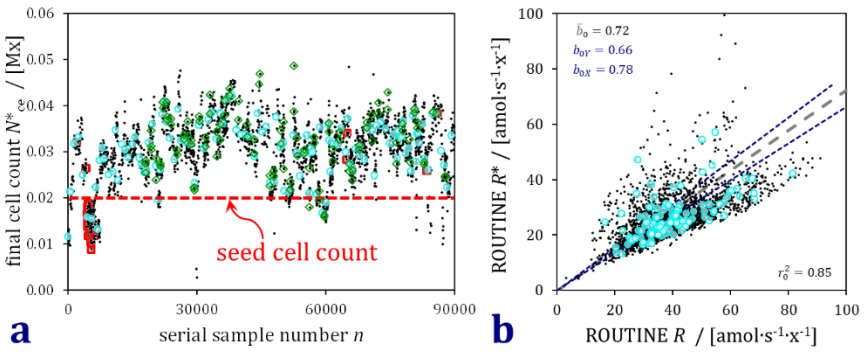

Figure 14. NHDF seed cell count versus final cell count in the XF96. Open circles: averages within plates (*N*=124). Dots: wells (*n*=2627). **(a)** Final cell count plotted over serial sample number. Red squares: cluster *l*C2 (*E*-*L*)/*E*<0.8 (Figure 10a,b), clustered in assays early in the sample series *n* and correlating with final cell counts that are lower than the seed cell count. Green diamonds: superimposed cluster *r*C2 (*R*-*L*)/*E*<0.04 (Figure 10d,e), evenly distributed across serial samples, but consistently appearing in two (47 plates) to three adjacent wells (6 plates). **(b)** Respiration *R** normalized for final cell count versus *R* normalized for seed cell count after removal of outliers. Lower *R** (*R** = 0.72·*R*) is due to normalization by the final cell count *N** which is 1.5 times higher than the seed cell count. Comparison of dots (wells) and circles (plates) indicates scatter between wells.

Two strategies are available for normalization for cell count. (*1*) The cell count is determined for seeding cells to the wells or injection of cells into the experimental chamber, abbreviated as 'seed count'. (*2*) The cell count is determined from the sample obtained from the well or experimental chamber, abbreviated as 'final count' when the cells are sampled at the end of the experimental run. The final cell count in the XF96 is on average 1.5 ± 0.3 (SD) times higher than the seed cell count (20 000 cells in a well; Figure 14). Consequently, normalization by the final cell count results in lower flow per cell and enhances the variability of the data (Figure 14b). Only the seed count is used for normalization in the present meta-analysis.

Acknowledgements
I thank Lucie Zdrazilova for input from our parallel manuscript, and Hans Zischka, Pablo M Garcia-Roves, Omar Torres-Quesada, Anthony JA Molina, Philip A Kramer, Jenny L Gonzalez-Armenta, Mateus Grings, and the Oroboros team — particularly Chris Donnelly, Timea Komlódi, Sabine Schmitt, Carolina Doerrier, and Luiza HD Cardoso — for stimulating discussions and critical comments. This work was partially funded by the European Union's Horizon 2020 research and innovation programme under grant agreement No. 859770, NextGen-O2k project. Contribution to the MitoEAGLE Task Group of the Mitochondrial Physiology Society.

Abbreviations
a: atto (10^{-18}); BC: bioenergetic cluster; BCA: bioenergetic cluster analysis; ce: living cell; E: noncoupled electron transfer state; E and E'_{tot}: ET capacity per cell *Rox*-corrected and total [amol·s^{-1}·x^{-1}]; ETS: electron transfer system; *FCR*: flux control ratio; HDF: human dermal fibroblasts; HFF: human foreskin fibroblasts (YP, young proliferating; GA, young growth-arrested; S, senescent); HRR: high-resolution respirometry; HSF: human skin fibroblasts (Y, young; A, aged); I_{O_2} (I_R, $I_{R'tot}$, I_L, $I_{L'tot}$, I_E, $I_{E'tot}$, I_{Rox}): O_2 flow in chamber [pmol·s^{-1}]; J_{V,O_2}: O_2 flux per chamber volume [pmol·s^{-1}·mL^{-1}]; L: LEAK state; L and L'_{tot}: LEAK respiration per cell *Rox*-corrected and total [amol·s^{-1}·x^{-1}]; M: mega (10^6); M: molar (mol·L^{-1}); n: number of technical repeats or total number of measurements; N: number of independent replica; N_{ce}: cell count, number of cells [x]; NHDF; normal human dermal fibroblasts; OCR: oxygen consumption rate; *OSI*: outlier-skewness index; p: pico (10^{-12}); R: ROUTINE state; R and R'_{tot}: ROUTINE respiration per cell *Rox*-corrected and total [amol·s^{-1}·x^{-1}]; ROX: residual oxygen consumption state; *Rox*: residual oxygen consumption per cell [amol·s^{-1}·x^{-1}]; SUIT: substrate-uncoupler-inhibitor titration; U: uncoupler; x: elementary unit; y: year.

References

Amrhein V, Greenland S, McShane B (2019) Scientists rise up against statistical significance. Nature 567:305-7.

Annesley SJ, Fisher PR (2019) Mitochondria in health and disease. Cells 8:680. doi: 10.3390/cells8070680

Curran-Everett D (2020) Evolution in statistics: *P* values, statistical significance, kayaks, and walking trees. Adv Physiol Educ 44:221-4.

de Mello AH, Costa AB, Engel JDG, Rezin GT (2018) Mitochondrial dysfunction in obesity. Life Sci 192:26-32. doi: 10.1016/j.lfs.2017.11.019

Dejmek J, Kohoutová M, Kripnerová M, Čedíková M, Tůma Z, Babuška V, Bolek L, Kuncová J (2018) Repeated exposure to hyperbaric hyperoxia affects mitochondrial functions of the lung fibroblasts. Physiol Res 67(Suppl 4):S633-S643.

Doane DP, Seward LE (2011) Measuring skewness: a forgotten statistic? J Statistics Education 19,2:1-18.

Doerrier C, Garcia-Souza LF, Krumschnabel G, Wohlfarter Y, Mészáros AT, Gnaiger E (2018) High-Resolution FluoRespirometry and OXPHOS protocols for human cells, permeabilized fibers from small biopsies of muscle, and isolated mitochondria. Methods Mol Biol 1782:31-70.

Eisenhauer JG (2003) Regression through the origin. Teaching Statistics 25:76-80.

Gellerich FN, Mayr JA, Reuter S, Sperl W, Zierz S (2004) The problem of interlab variation in methods for mitochondrial disease diagnosis: enzymatic measurement of respiratory chain complexes. Mitochondrion 4:427-39.

Gnaiger E (2001) Bioenergetics at low oxygen: dependence of respiration and phosphorylation on oxygen and adenosine diphosphate supply. Respir Physiol 128:277-97.

Gnaiger E (2008) Polarographic oxygen sensors, the oxygraph and high-resolution respirometry to assess mitochondrial function. In: Mitochondrial Dysfunction in Drug-Induced Toxicity (Dykens JA, Will Y, eds) John Wiley & Sons, Inc, Hoboken, NJ:327-52.

Gnaiger E (2020) Mitochondrial pathways and respiratory control. An introduction to OXPHOS analysis. 5th ed. Bioenerg Commun 2020.2: 112 pp. doi:10.26124/bec:2020-0002.

Gnaiger E (2021) The elementary unit - canonical reviewer's comments on: Bureau International des Poids et Mesures (2019) The International System of Units (SI) 9th ed. MitoFit Preprints 2020.4.v2. doi:10.26124/mitofit:200004.v2

Gnaiger E et al — MitoEAGLE Task Group (2020) Mitochondrial physiology. Bioenerg Commun 2020.1. doi:10.26124/bec:2020-0001.v1

Greco M, Villani G, Mazzucchelli F, Bresolin N, Papa S, Attardi G (2003) Marked aging-related decline in efficiency of oxidative phosphorylation in human skin fibroblasts. FASEB J 17:1706-8.

Han Y, Zhou S, Coetzee S, Chen A (2019) SIRT4 and its roles in energy and redox metabolism in health, disease and during exercise. Front Physiol 10:1006. doi: 10.3389/fphys.2019.01006

Herst PM, Rowe MR, Carson GM, Berridge MV (2017) Functional mitochondria in health and disease. Front Endocrinol (Lausanne) 8:296. doi: 10.3389/fendo.2017.00296.

Hood DA, Memme JM, Oliveira AN, Triolo M (2019) Maintenance of skeletal muscle mitochondria in health, exercise, and aging. Annu Rev Physiol 81:19-41. doi: 10.1146/annurev-physiol-020518-114310

Hütter E, Renner K, Pfister G, Stöckl P, Jansen-Dürr P, Gnaiger E (2004) Senescence-associated changes in respiration and oxidative phosphorylation in primary human fibroblasts. Biochem J 380:919-28.

Jaber SM, Yadava N, Polster BM (2020) Mapping mitochondrial respiratory chain deficiencies by respirometry: beyond the Mito Stress Test. BM Exp Neurol 328:113282.

Kahneman D (2011) Thinking, fast and slow. Penguin Books 499 pp.

Karabatsiakis A, Boeck C, Salinas-Manrique J, Kolassa S, Calzia E, Dietrich DE, Kolassa IT (2014) Mitochondrial respiration in peripheral blood mononuclear cells correlates with depressive subsymptoms and severity of major depression. Transl Psychiatry 4:e397.

Kozieł R, Greussing R, Maier AB, Declercq L, Jansen-Dürr P (2011) Functional interplay between mitochondrial and proteasome activity in skin aging. J Invest Dermatol 131:594-603.

Kuffner K, Triebelhorn J, Meindl K, Benner C, Manook A, Sudria-Lopez D, Siebert R, Nothdurfter C, Baghai TC, Drexler K, Berneburg M, Rupprecht R, Milenkovic VM, Wetzel CH (2020) Major depressive disorder is associated with impaired mitochondrial function in skin fibroblasts. Cells 9:884. doi: 10.3390/cells9040884

Mahapatra G, Smith SC, Hughes TM, Wagner B, Maldjian JA, Freedman BI, Molina AJA (2018) Blood-based bioenergetic profiling is related to differences in brain morphology in African Americans with Type 2 diabetes. Clin Sci (Lond) 132:2509-18.

Memme JM, Erlich AT, Phukan G, Hood DA (2021) Exercise and mitochondrial health. J Physiol 599:803-17. doi: 10.1113/JP278853

Miettinen TP, Björklund M (2017) Mitochondrial function and cell size: an allometric relationship. Trends Cell Biol 27:393-402.

Nunnari J, Suomalainen A (2012) Mitochondria: in sickness and in health. Cell 148:1145-59. doi: 10.1016/j.cell.2012.02.035

Renner K, Amberger A, Konwalinka G, Gnaiger E (2003) Changes of mitochondrial respiration, mitochondrial content and cell size after induction of apoptosis in leukemia cells. Biochim Biophys Acta 1642:115-23.

Savage VM, Allen AP, Brown JH, Gillooly JF, Herman AB, Woodruff WH, West GB (2007) Scaling of number, size, and metabolic rate of cells with body size in mammals. Proc Natl Acad Sci U S A 104:4718-23.

Schöpf B, Weissensteiner H, Schäfer G, Fazzini F, Charoentong P, Naschberger A, Rupp B, Fendt L, Bukur V, Giese I, Sorn P, Sant'Anna-Silva AC, Iglesias-Gonzalez J, Sahin U, Kronenberg F, Gnaiger E, Klocker H (2020) OXPHOS remodeling in high-grade prostate cancer involves mtDNA mutations and increased succinate oxidation. Nat Commun 11:1487.

Silver N (2012) The signal and the noise. The art and science of prediction. Penguin Press:534 pp.

Steinlechner-Maran R, Eberl T, Kunc M, Margreiter R, Gnaiger E (1996) Oxygen dependence of respiration in coupled and uncoupled endothelial cells. Am J Physiol Cell Physiol 271:C2053-61.

Ulrich R, Miller J (2020) Meta-research: Questionable research practices may have little effect on replicability. Elife 9:e58237. doi: 10.7554/eLife.58237

Villani G, Attardi G (1997) In vivo control of respiration by cytochrome c oxidase in wild-type and mitochondrial DNA mutation-carrying human cells. Proc Natl Acad Sci U S A 94:1166-71.

Wagner BA, Venkataraman S, Buettner GR (2011) The rate of oxygen utilization by cells. Free Radic Biol Med 51:700-12.

Wallace DC, Fan W, Procaccio V (2010) Mitochondrial energetics and therapeutics. Annu Rev Pathol 5:297-348.

Wilcox RR (2015) Comparing the variances of two dependent variables. Journal of Statistical Distributions and Applications 2:7. doi:10.1186/s40488-015-0030-z

Wu M, Neilson A, Swift AL, Moran R, Tamagnine J, Parslow D, Armistead S, Lemire K, Orrell J, Teich J, Chomicz S, Ferrick DA (2007) Multiparameter metabolic analysis reveals a close link between attenuated mitochondrial bioenergetic function and enhanced glycolysis dependency in human tumor cells. Am J Physiol Cell Physiol 292:C125-36.

Yépez VA, Kremer LS, Iuso A, Gusic M, Kopajtich R, Koňaříková E, Nadel A, Wachutka L, Prokisch H, Gagneur J (2018) OCR-Stats: Robust estimation and statistical testing of mitochondrial respiration activities using Seahorse XF Analyzer. PLOS ONE 13:e0199938. https://doi.org/10.1371/journal.pone.0199938

Zdrazilova L, Hanskova H, Gnaiger E (2021) Comparable respiratory activity in attached and suspended fibroblasts. MitoFit Preprints 2021.7. doi:10.26124/mitofit:2021-0007

Zhang X, Yuan T, Keijer J, de Boer VCJ (2021) OCRbayes: a Bayesian hierarchical modeling framework for Seahorse extracellular flux oxygen consumption rate data analysis. PLOS ONE 16:e0253926. https://doi.org/10.1371/journal.pone.0253926